# A new IR–Array photometric survey of Galactic Globular Clusters: A detailed study of the RGB sequence as a step towards the global testing of stellar models. <sup>1</sup>

Francesco R. Ferraro

European Southern Observatory, Karl Schwarzschild Str. 2, D–85748 Garching bei München, Germany

On leave from Osservatorio Astronomico di Bologna e-mail: fferraro@eso.org, ferraro@bo.astro.it

and

Paolo Montegriffo, Livia Origlia Osservatorio Astronomico di Bologna, Via Ranzani 1, I–40127 Bologna, Italy e–mail: pmontegr,origlia@bo.astro.it

and

Flavio Fusi Pecci Stazione Astronomica, 09012 Capoterra, Cagliari, Italy On leave from Osservatorio Astronomico di Bologna. e-mail: flavio@bo.astro.it

## **ABSTRACT**

We present high quality near infrared Color Magnitude Diagrams of 10 Galactic Globular Clusters (GCs) spanning a wide metallicity range (-2.15 < [Fe/H] < -0.2). This homogeneous data—base has been used to perform a detailed analysis of the Red Giant Branch (RGB), adopting a variety of observables to describe its physical and chemical properties.

First, a set of metallicity indicators have been measured, namely: (i) the RGB (J–K) and (V–K) colors at different magnitude levels; (ii) the RGB K magnitude at different colors; (iii) the RGB slope. For these parameters we present new calibrations in terms of both spectroscopic iron abundance and global metallicity, including the  $\alpha$ –element enhancement. These relations can be used to derive a photometric estimate of the GC metal content from the RGB morphology and location.

Second, the location in luminosity of the main RGB features (namely, the Bump and the Tip) and their dependence on metallicity have been studied, yielding quantitative observational relationships.

Finally, adopting new transformations between the observational and theoretical quantities, the mean ridge lines for the clusters of our sample have been reported in

 $<sup>^{\</sup>rm 1}$  Based on data taken at the ESO–MPI 2.2m Telescope equipped with the near IR camera IRAC2 - ESO, La Silla (Chile).

the  $(M_{Bol}, Log(T_e))$  plane. This allows to study the RGB location in terms of effective temperature, bolometric luminosity of the main RGB features, and their calibrations with varying metallicity. Direct comparisons between up–dated theoretical models and observations show an excellent overall agreement.

Subject headings: techniques: photometric — surveys — stars: fundamental parameters – stars: late—type – stars: Population II

#### 1. Introduction

Stellar evolution theory is crucial to yield a reliable clock for dating astrophysical objects. Suitable Color Magnitude Diagrams (CMDs) and Luminosity Functions (LFs) are the most powerful tools to test theoretical models and, in turn, the *running* of the stellar clock. Within this framework, our group started a long–term project devoted to the quantitative analysis and testing of each individual evolutionary sequence in the CMDs of Galactic Globular Clusters (GGCs).

In this paper we present the results of a detailed study of the Red Giant Branch (RGB), using CMDs and LFs in the near–IR bands. Since the contrast between the red giants and the unresolved background population in the IR bands is greater than in any optical region, they can be observed with the highest S/N ratio also in the innermost region of the cluster. Moreover, when combined with optical observations, IR magnitudes provide useful observables such as for example the V–K color, which is an excellent indicator of the stellar effective temperature ( $T_e$ ).

The advantage of observing GGCs in the near IR is well known since many years. The first systematic IR survey of GGCs was carried out in their pioneering work by Frogel, Cohen & Persson (1983, hereafter FCP83), which provided in particular the first quantitative description of the RGB location with varying the cluster metal abundance. However, due to intrinsic technical limits of the old single—channel detectors and aperture photometry, the FCP83 data—base includes only a few bright stars in the external regions of the clusters (a total of  $\sim 350$  stars in 30 GGCs). A detailed comparison with the theoretical models based on suitable LFs was thus actually impossible because of the small number of observed stars.

The advent of new IR arrays with pixel sizes and overall performances close to those of optical CCDs has then opened new perspectives to the construction of large and complete samples of RGB stars with high photometric accuracy (Davidge & Simons 1991, 1994a,b; Minniti 1995, Minniti et al. 1995, Ferraro et al. 1994a,b, Ferraro et al. 1995, Montegriffo et al. 1995, Kuchinski et al. 1995—hereafter K95, Kuchinski & Frogel 1995—hereafter KF95, Guarnieri et al. 1998).

The main aim of our project is to obtain a complete quantitative description of the RGB as a function of the intrinsic cluster parameters, and to yield a few observational relationships for general use and suitable to carefully test the theoretical models. Schematically, we study:

- i) the location in color of the RGB, its morphology and slope, and their dependence on metal abundance.
- ii) the extent in luminosity of the RGB; this provides a quantitative determination of the stellar luminosity at the helium-flash (the RGB-tip) with varying metallicity, setting also strong constraints on mass loss and the calibration of a useful method to determine the cluster distance scale.

iii) the precise location in luminosity and temperature of the so-called RGB bump and of any other peculiarity (gaps, clumps, etc.) one might detect in the available data.

The calibrations eventually obtained depend on the adopted reddening, metallicity and distance scale, and on the assumed transformations between the observed and theoretical planes (especially the bolometric corrections and the temperature scale).

In Sect.2 we present the IR data of the selected sample of GGCs. A wider presentation of some individual clusters can be found in Ferraro et al. (1994a), Montegriffo et al. (1995) and Guarnieri et al. (1998). In Sect.3 we describe the procedure used to compute the fiducial RGB ridge lines. In Sect.4 we present the basic assumptions on metallicity scales, distance modulus and reddening adopted in this paper. In Sect.5 we analyze the general RGB location and morphology in the observational planes. In Sect.6 we present our results on the observed RGB features and the comparison with previous work and up—dated theoretical models. In Sect.7 we discuss the transformations to the theoretical plane and in Sect.8 we summarize our conclusions.

# 2. The Sample

The IR data set of globular clusters presented here was obtained at ESO, La Silla (Chile), during two different runs (on June 1992 and June 1993), using the ESO–MPI 2.2m telescope and the near IR camera IRAC–2 (Moorwood et al. 1992) equipped with a NICMOS–3 256x256 array detector. The frames were taken through standard J and K broad-band filters. For each cluster we mapped the central  $4 \times 4$  square arcminutes using two different magnifications: 0.27"/pixel in the central field, and 0.5"/pixel for the four partially overlapping fields centered at  $\sim$ 100 arcsec NE, NW, SW and SE, respectively, from the cluster center. In the case of M4 only the central high spatial resolution frames were used.

The resulting images were averages of typically 60 exposures of 1 sec integration time each, and were sky subtracted and flat-field corrected. The sky was monitored every 2 minutes at a distance of about 300 arcsec from the cluster center.

More details on the pre-reduction procedure and the photometric calibration can be found in Ferraro et al. (1994a) and Montegriffo et al. (1995). Here we just remark that most of the photometric reductions were carried out using the ROMAFOT package (Buonanno et al. 1983), specifically adapted to work with undersampled stellar images (Buonanno & Iannicola, 1988).

The calibration curves linking the aperture photometry to the standard system are reported in Ferraro et al. (1994a) and Montegriffo et al. (1995) for the June 1992 and June 1993 runs, respectively. During these two runs we secured images of a sample of 15 GGCs but here we present the results for the 10 GGCs (namely M15, M30, M68, M55, M4, M107, M69, 47 Tuc, NGC6553, NGC6528) with the best quality data: the total sample contains J and K photometry of about 17000 stars. The V magnitude used to derive the V–K color is taken from recent published photometry, according to Table 1 by Montegriffo et al. (1998).

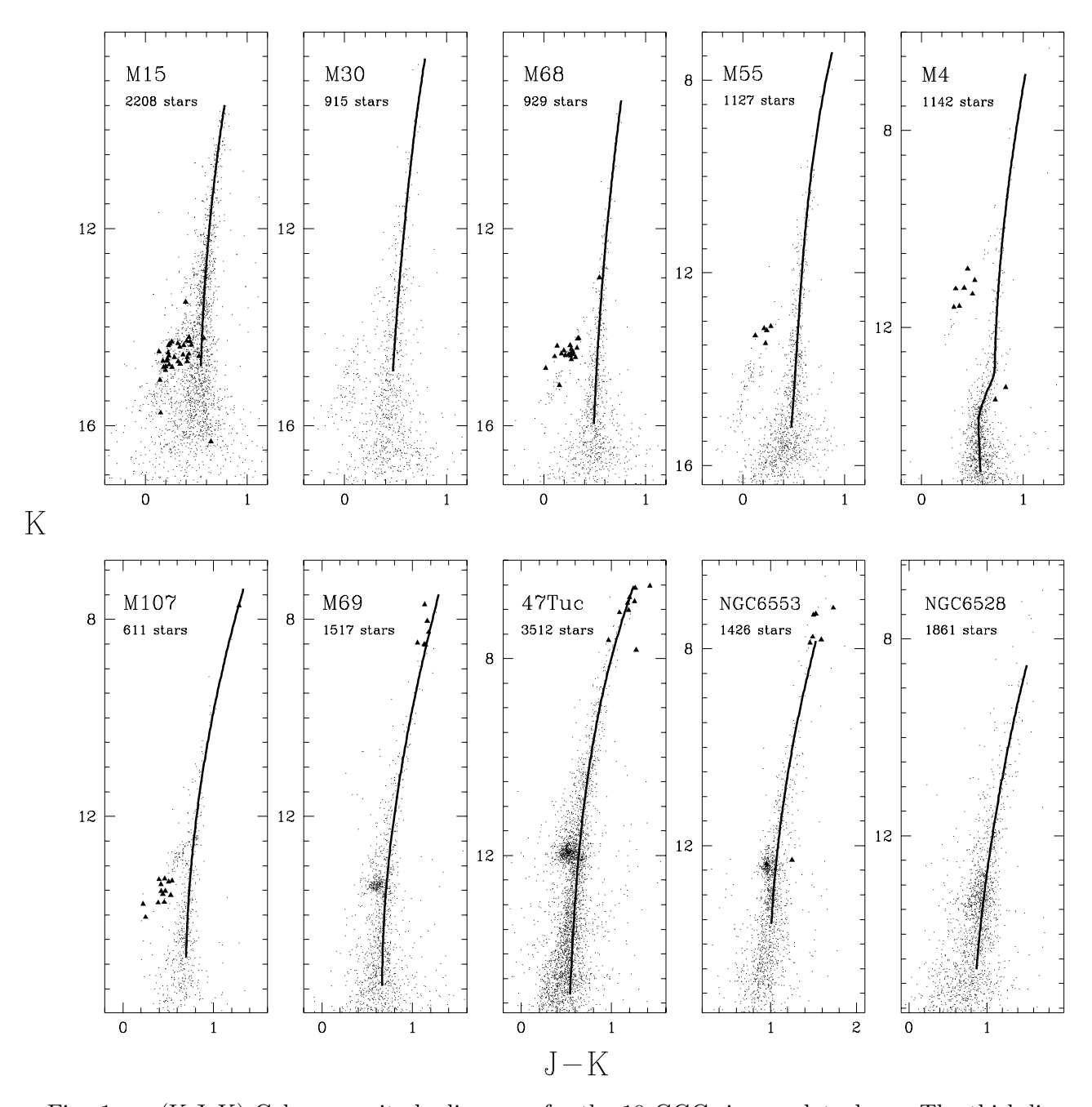


Fig. 1.— (K,J–K) Color–magnitude diagrams for the 10 GGCs in our data–base. The thick line in each panel indicates the fiducial ridge line of the RGB. Variable stars have been plotted as filled triangles.

# 3. The RGB fiducial ridge lines

In order to compute the fiducial RGB ridge lines for the clusters in our sample we followed a standard procedure already used by other authors (Da Costa & Armandroff 1990; Ferraro et al.

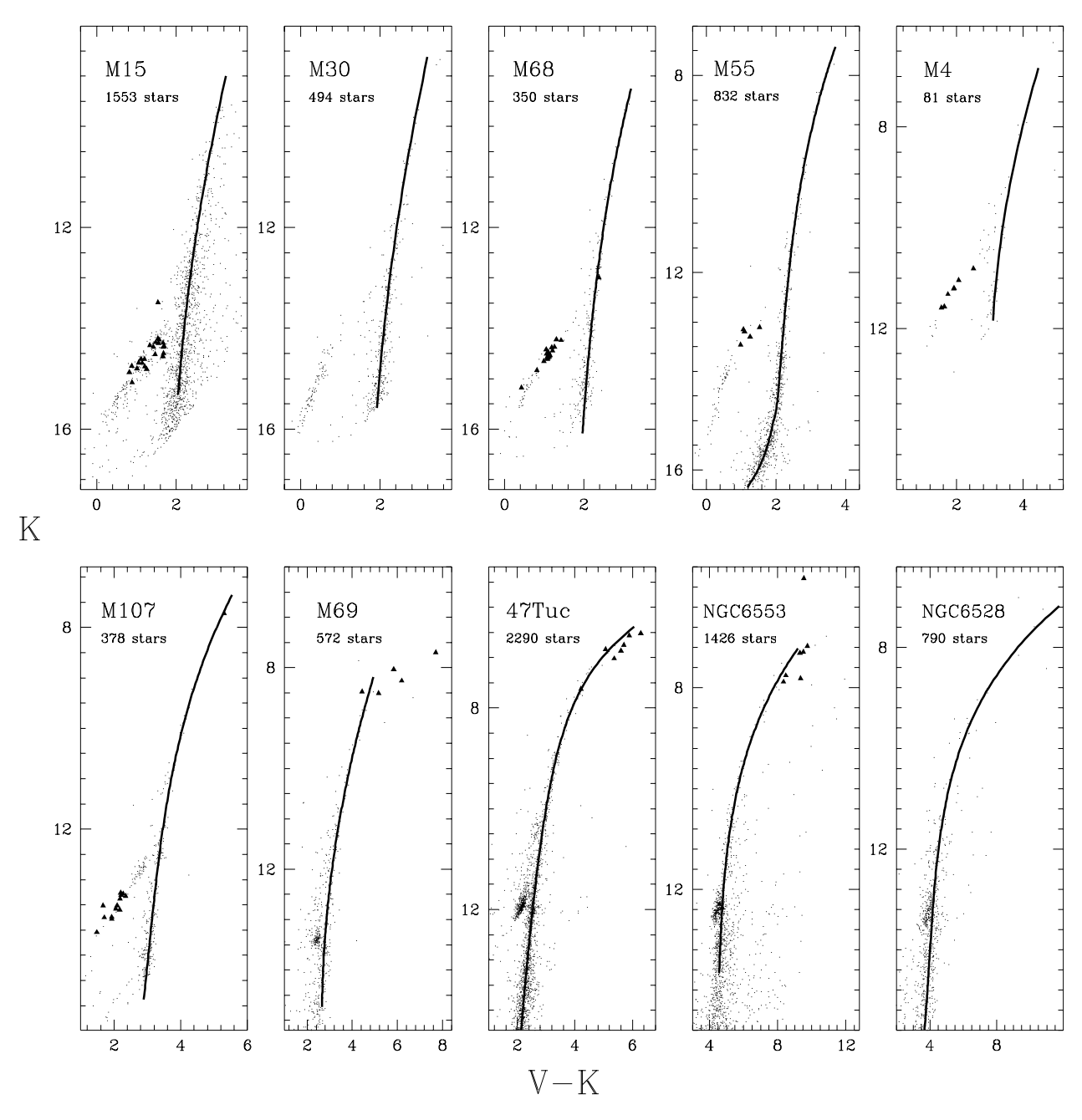


Fig. 2.— (K,V–K) Color–magnitude diagrams for the 10 GGCs in our data–base. The thick line in each panel indicates the fiducial ridge line of the RGB. Variable stars have been plotted as filled triangles.

# 1999, hereafter F99).

A first rough selection of the candidate RGB stars was performed on the CMDs by eye, removing the HB and part of the AGB stars. This operation is relatively easy for all the clusters

of our sample (cf. Fig.1,2), except the most metal rich ones, like NGC6528, where the HB merges the RGB without displaying any discontinuity.

As a second step, we used a low order polynomial to fit the selected stars and we rejected those at  $\geq \pm 2\sigma$  from the best fit line. The procedure was iterated until the best stable fit to the overall shape of the RGB was obtained.

The final ridge lines overplotted to the (K,J–K) and (K,V–K) CMDs are shown in Fig.1 and Fig.2, respectively.

Cluster		$[Fe/H]_{Z85}$	$[Fe/H]_{CG97}$	[M/H]	E(B-V)	V(ZAHB)	$(m - M)_0$
NGC104	47Tuc	-0.71	-0.70	-0.59	$0.04 \pm 0.02$	$14.22\pm0.07$	13.32
NGC4590	M68	-2.09	-1.99	-1.81	$0.04 \pm 0.02$	$15.75\pm0.05$	15.14
NGC6121	M4	-1.33	-1.19	-0.94	$0.36 \pm 0.05$	$13.45 \pm 0.10$	11.68
NGC6171	M107	-0.99	-0.87	-0.70	$0.33 \pm 0.05$	$15.72 \pm 0.10$	13.95
NGC6528		-0.23	-0.38	-0.31	$0.62 \pm 0.10$	$17.17 \pm 0.20$	14.37
NGC6553		-0.29	-0.44	-0.36	$0.84 \pm 0.10$	$16.92 \pm 0.20$	13.46
NGC6637	M69	-0.59	-0.68	-0.55	$0.17 \pm 0.04$	$15.95 \pm 0.10$	14.64
NGC6809	M55	-1.81	-1.61	-1.41	$0.07 \pm 0.04$	$14.60 \pm 0.10$	13.82
NGC7078	M15	-2.17	-2.12	-1.91	$0.09 \pm 0.04$	$15.90 \pm 0.07$	15.15
NGC7099	M30	-2.13	-1.91	-1.71	$0.03 \pm 0.02$	$15.30\pm0.10$	14.71

Table 1. Adopted parameters for the observed GGCs.

Note. — Global metallicity ([M/H]), V(ZAHB) and  $(m-M)_0$  are from Ferraro et al. (1999).

#### 4. Basic assumptions

In this Section we discuss the basic assumptions and the corresponding uncertainties on the adopted metallicity scales, distance moduli and reddening for the clusters in our sample and their impact on the determination of the RGB parameters.

# 4.1. The cluster metallicity

The metallicity measurements most frequently used for GGCs refer to the classical scale proposed by Zinn and collaborators in the 80's (Zinn 1980, Zinn & West 1984, Zinn 1985, hereafter Z85). Even though new homogeneous observations of metallicity indicators have been obtained (cf. e.g. Carretta & Gratton, 1997 – hereafter CG97 – Rutledge, Hesser & Stetson 1997), the Zinn's scale still represents the most complete data—set available in the literature. There are however reasons, discussed in the recent quoted papers, which suggest to slightly revise the Zinn's scale according to the latest high—resolution spectral data.

In particular, CG97 have recently presented high quality measurements of iron abundances using high dispersion spectra of FeI and FeII lines. They observed stars in a sample of 24 GGCs

spanning the metallicity range -2.24 < [Fe/H] < -0.5. By comparing their measurements with those published by Z85, they noted that there are systematic differences (up to  $\delta[Fe/H] \sim 0.2$ ) with respect to the Z85 scale, especially for intermediate metallicities ( $[Fe/H] \sim -1.5$ ). CG97 derived a quadratic relation to transform the Z85 data in their own scale (cf. their eq. 7), which we will adopt in the following as reference. Consequently, since only 5 out of 10 GGCs considered in this paper have direct measurements in the GC97 list, for the other 5 the metallicity has been obtained by transforming the Z85 estimate into the GC97 scale (cf. F99).

A further consideration is important: in order to perform a correct parametrization of the RGB behavior as a function of metallicity, the simple knowledge of the quantity usually called *iron abundance* is not sufficient. In fact, it is known since many years (Renzini 1977) that the scaling of the RGB location in the CMD with metallicity is essentially due to the changing of the stellar opacity.

The main source of the continuum opacity in the temperature range 3000–6000K, typical of the old RGB population of GGCs, are the  $H^-$  ions. They form by capturing the electrons provided by metals with a low–ionization potential (mainly Mg, Si, Fe). For this reason, as noted among others by Straniero & Chieffi (1991), and Salaris & Cassisi (1996), the RGB location mainly depends on the [Mg+Si+Fe] mixture abundance rather than on the [Fe] abundance alone. Therefore, a more reliable parameter to describe the actual metal content of the RGB stars is the so–called global metallicity, which takes into account not only the iron but also the the  $\alpha$ –element (like Mg and Si) abundance.

There are many observational evidences (cf. e.g. Carney 1996 and references therein) that  $\alpha$ —elements are enhanced with respect to iron in Population II stars. While there is a quite general consensus on the size of the mean overabundance ( $[\alpha/\text{Fe}]\sim0.3$  dex), the actual trend with metallicity is not firmly established (cf. Carney 1996 and Origlia et al. 1997 for references).

Straniero & Chieffi (1991) and Salaris, Chieffi & Straniero (1993) demonstrated that, when computing the isochrones of Population II stars, the contribution of the  $\alpha$ -element enhancement can be taken into account by simply re–scaling standard models to the *global* metallicity [M/H] according to the following relation:

$$[M/H] = [Fe/H] + log_{10}(0.638f_{\alpha} + 0.362)$$

where  $f_{\alpha}$  is the enhanced factor of the  $\alpha$ -elements.

Following these prescriptions, in F99 we computed the global metallicity for a sample of 61 GGCs within the framework of a systematic study of the evolved sequences in the (V,B–V) CMD. The values assumed here and listed in Table 1 have been thus taken from Table 2 in F99. Schematically, in F99 we assumed a constant  $[\alpha/Fe] = 0.28$  for [Fe/H] < -1 and linearly decreasing to zero for -1 < [Fe/H] < 0. We also carefully discussed there the possible effect of different assumptions in the  $\alpha$ -enhancing relation. In particular, we showed that, adopting a constant enhancement over the entire range of metallicity (-2 < [Fe/H] < 0) (Carney 1996) rather than a linear decreasing trend for [Fe/H] > -1, does not produce any significative difference in the description of the main RGB features in the (V,B–V) plane.

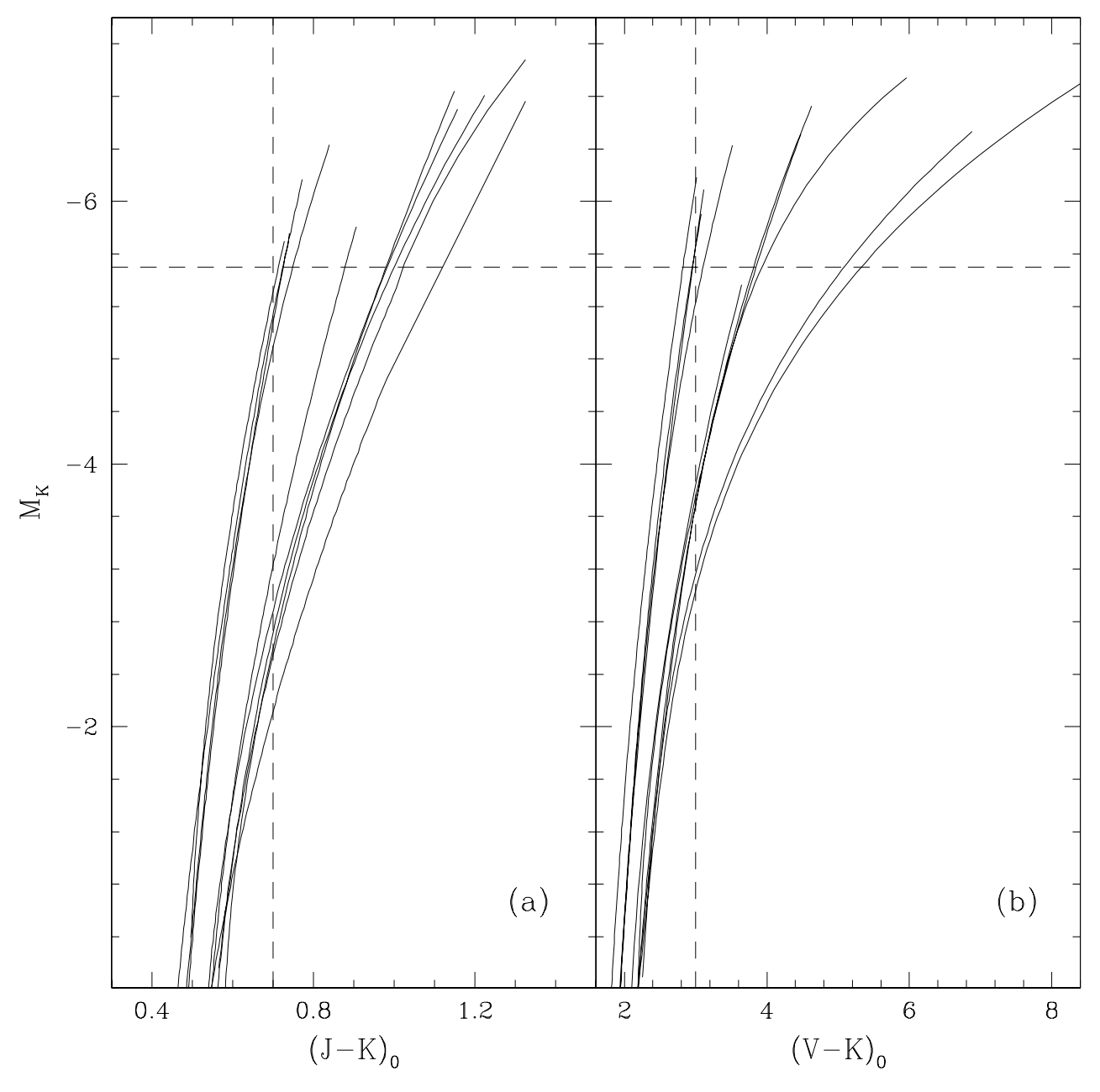


Fig. 3.— RGB fiducial ridge lines for the 10 GGCs in our sample in the  $M_K$ ,  $(J-K)_0$  and  $M_K$ ,  $(V-K)_0$  planes,  $(panel\ (a)\ and\ (b))$ , respectively. The dashed lines indicate the magnitude levels at which some of the parameters defined in the text are read.

# 4.2. The distance scale and reddening

To convert the RGB fiducial lines into the absolute planes it is necessary to adopt a distance scale and to correct for reddening.

Despite the huge observational efforts, the definition of the most suitable distance scale for GGCs is still very controversial and beyond the purposes of the present study (see for discussion and references VandenBerg et al. 1996, Chaboyer et al. 1996, Gratton et al. 1997, Caloi et al. 1997, Reid 1998, Pont et al. 1998, Carretta et al. 1999).

In the following we adopt the distance scale discussed and eventually established in F99. In that paper a new methodology to derive the actual level of the ZAHB and the distance moduli from the matching of V(ZAHB) and the theoretical models computed by Straniero, Chieffi & Limongi (1997, hereafter SCL97) has been presented.

The theoretical relation adopted by F99 for the ZAHB is the following:

$$M_V^{ZAHB} = 0.0458[Fe/H]^2 + 0.3485[Fe/H] + 1.0005$$

which, in the range -2.2 < [M/H] < -0.4, can also be described by the linear best-fit regression:

$$M_V^{ZAHB} = 0.23([Fe/H] + 1.5) + 0.595$$

Among the many possible choices within the range of the so-called *long* and *short* distances scales (see references above), this relation yields intermediate values for the GGC distance moduli.

The reddening corrections have been computed using the latest compilation by Harris (1996). In Table 1, the final metallicity (cf. Sect.4), reddening (Harris 1996) and distance modulus (from F99, Table 2, column 7) adopted in this paper for the 10 GGCs in our sample are reported.

The impact of different assumptions for the cluster distance scale and reddening will be discussed in Sect. 6.1.1 and 6.1.2.

### 4.3. Errors

Though the uncertainty in the determination of the observable V(ZAHB) is  $\sim 0.1$  mag (see column 6 in Table 1) for most of the clusters in our sample, according to F99 we conservatively estimate that the global uncertainty on the derived distance moduli listed in Table 1 is of the order of  $\sim 0.2$  mag. This estimate takes also into account the effect of the errors in the adopted metal abundances, reddening etc.. The distance modulus uncertainty turns to be the driving factor in the error budget of most of the RGB parameters derived in this paper, affecting both the determination of the absolute magnitude at which the RGB colors are measured and the absolute (and then bolometric) magnitude of the RGB bump and tip. Thus our generous estimate of the distance modulus error yields also conservative estimates of RGB parameter uncertainties.

It is more difficult to evaluate the reddening error for each individual cluster. However, by comparing the values quoted in different catalogs, we derive an average uncertainty of a few hundredths of magnitude, the largest values being those relative to the two most metal rich clusters in our sample (namely NGC6553 and NGC6528).

#### 5. The RGB location and morphology: definitions

Since the main purpose of this paper is the detailed study of the RGB properties using suitable CMDs, special care is devoted to properly define and measure: i) the parameters describing the

RGB location in color and in magnitude and *ii*) the parameters describing the RGB morphology, since they represent the most general and widely used descriptors of the RGB in any resolved stellar population.

#### 5.1. The RGB location in color and in magnitude

Many different observables have been defined and used to locate the RGB in the classical V,B–V plane (cf. F99 and reference therein), in the V,V–I plane (Da Costa & Armandroff 1990) and in the IR planes (cf. e.g. FCP83).

FCP83 originally defined  $(V-K)_0$  (RGB) and  $(J-K)_0$  (RGB) as the colors of the mean RGB ridge line measured at  $M_K$ =-5.5. Afterwards, the RGB colors have been measured at different magnitude levels ( $M_K$ =-5.0 and  $M_K$ =-4.0, cf. Cohen & Sleeper 1995, hereafter CS95) and the importance of such an approach is nicely illustrated by CS95 (cf. e.g. their Figure 3). In the observational plane, the color difference among mean ridge lines for clusters of different metallicity becomes progressively more and more pronounced ascending the RGB up to the Tip, due to the the molecular blanketing effects.

FCP83 also defined the  $M_{K_0}$  (RGB) as the RGB luminosity at constant color  $(V-K)_0=3.0$ . This parameter samples different RGB regions depending from the cluster metallicity: while in metal–poor clusters  $M_K$  at  $(V-K)_0=3$  marks the bright upper branch, in the metal–rich ones it intersects the intermediate RGB, slightly brighter than the HB level.

To properly map the overall behavior of the RGB as a function of the metallicity, in the following we measure the  $(J-K)_0$  and  $(V-K)_0$  colors at different magnitudes:  $M_K=-3$ , -4, -5 and -5.5, and the magnitude  $M_{K_0}$  (RGB) at fixed color in both the  $[M_K, (J-K)_0]$  and  $[M_K, (V-K)_0]$  planes, respectively.

#### 5.2. The RGB slope

The shape of the RGB in a GGC is sensitive to the abundance of heavy elements and substantially insensitive to the age and Helium abundance (cf. Figure 13 by K95). Moreover, the sensitivity of the RGB slope to the metallicity is highly pronounced in the observational plane, since an enhancement of the molecular blanketing strongly affects the RGB colors, making extremely red the coolest and brightest stars. Consequently, the RGB slope is a powerful metallicity indicator as shown for example by Ortolani, Barbuy & Bica (1991) and K95 (cf. their Figure 15).

K95 presented JHK photometry of 4 high metallicity GGCs (namely NGC5927, NGC6712, M71 and Terzan 2). Using this sample and data previously published for other two clusters (47 Tuc, Frogel et al. 1981; M69, Davidge & Simons 1991 and FCP83), they derived the RGB slopes in the K,(J–K) plane by fitting the upper part of the RGB (only the stars between 0.6 and 5.1 mag brighter than the Zero Age Horizontal Branch (ZAHB) level in K were considered).

They proposed equations in the form J–K=b+a×K (cf. their Table 9), and also correlated the RGB slope with the metallicity, finding the relation:  $[Fe/H] = -3.9 - 24.85 \ slope_{RGB}$ . This relation has been later refined by KF95 who found:  $[Fe/H] = -2.89 - 23.84 \ slope_{RGB}$ . In the present study we derive similar relations for the RGB slope in the K,J–K plane from our sample of

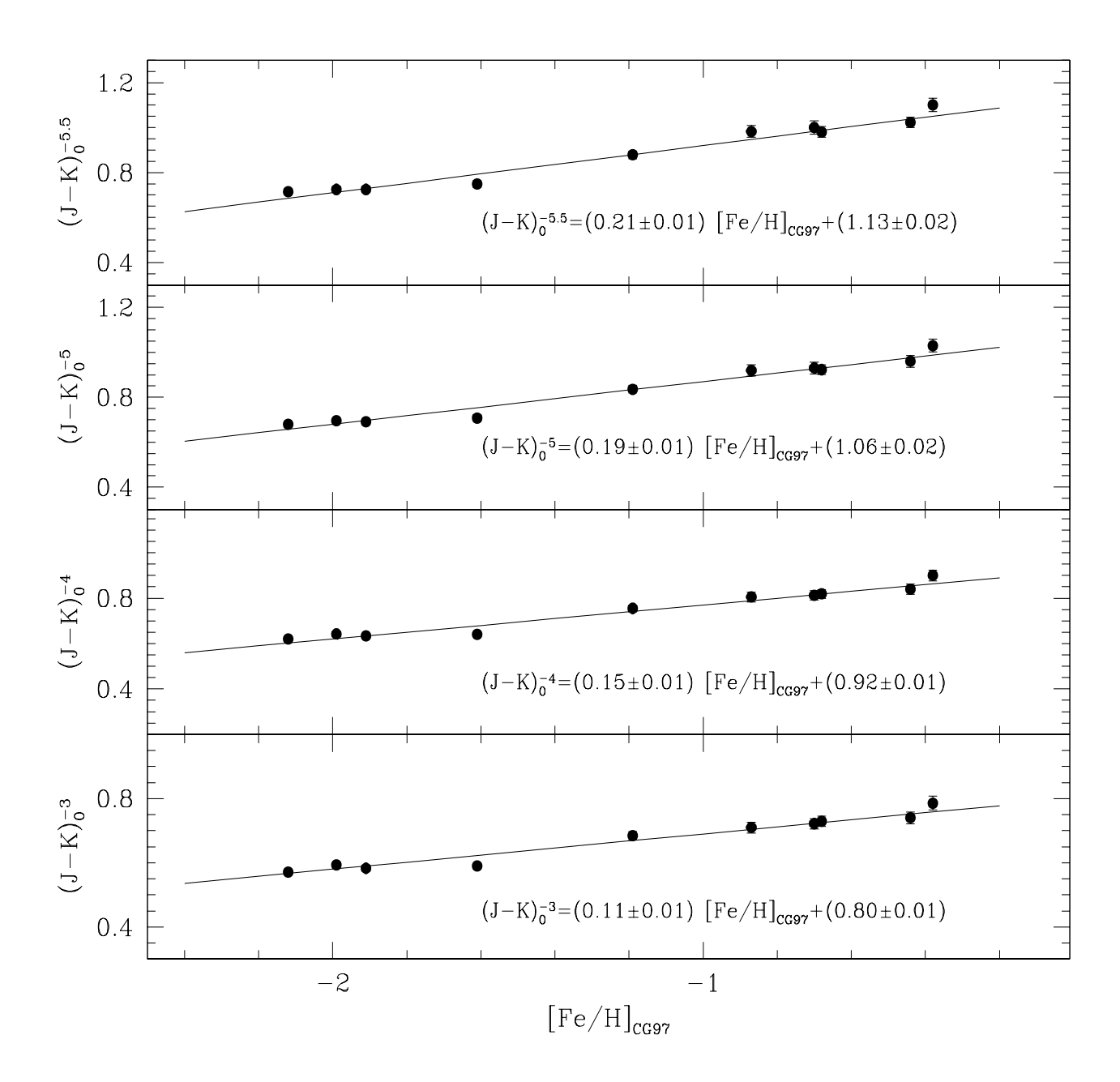


Fig. 4.— RGB mean  $(J-K)_0$  color at different  $M_K$  (-3, -4, -5, -5.5) as a function of CG97 metallicity for the 10 GGCs in our sample.

GGCs.

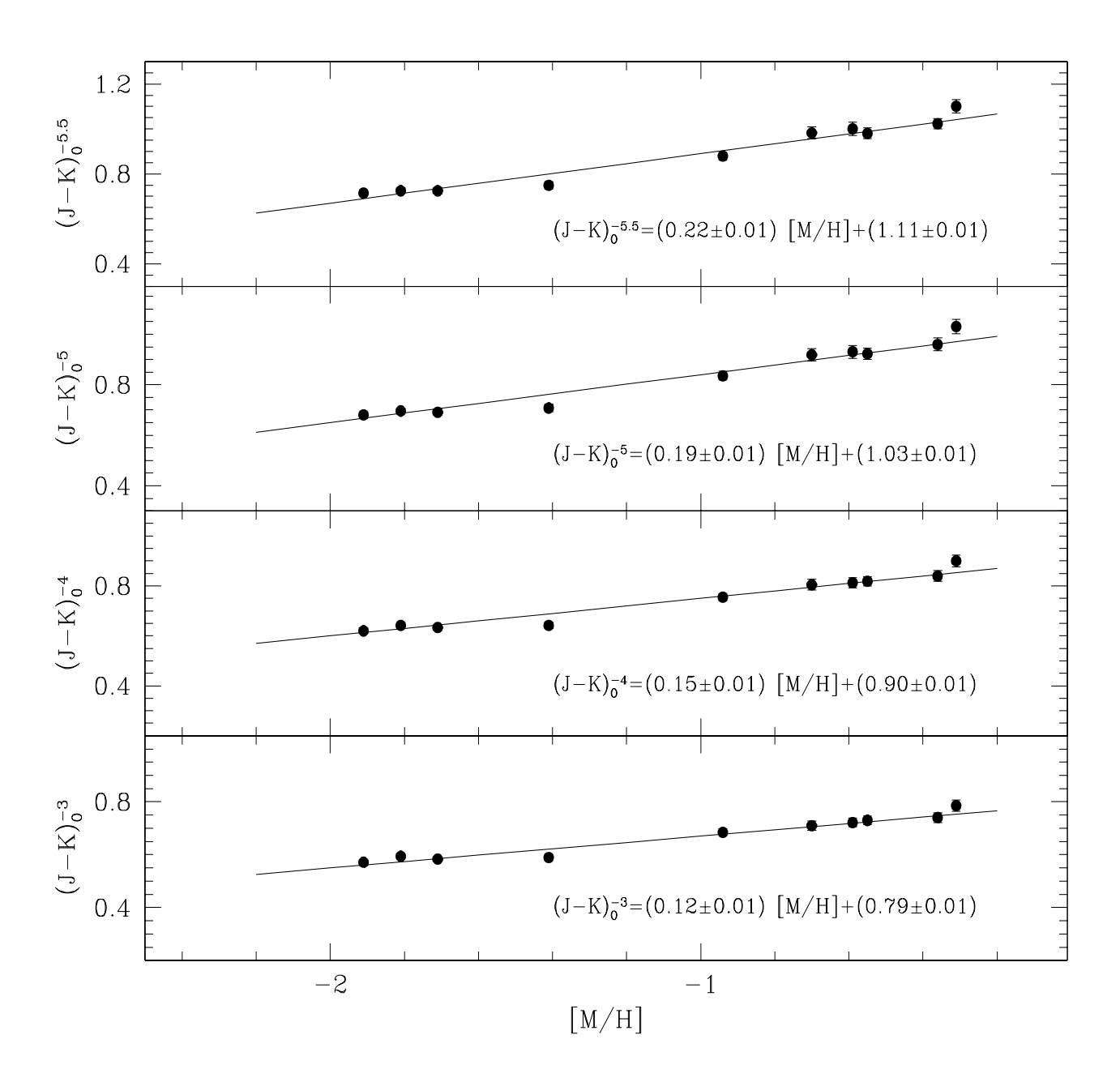


Fig. 5.— As in Fig.4 but for the *global* metallicity scale.

## 6. The RGB features: measurements

In order to perform a complete characterization of the RGB, in this section we calibrate the main RGB observables in the IR-CMDs (namely colors at fixed magnitudes, magnitudes at fixed colors, slope, bump and tip) and discuss their dependence on metallicity. In doing this we use the

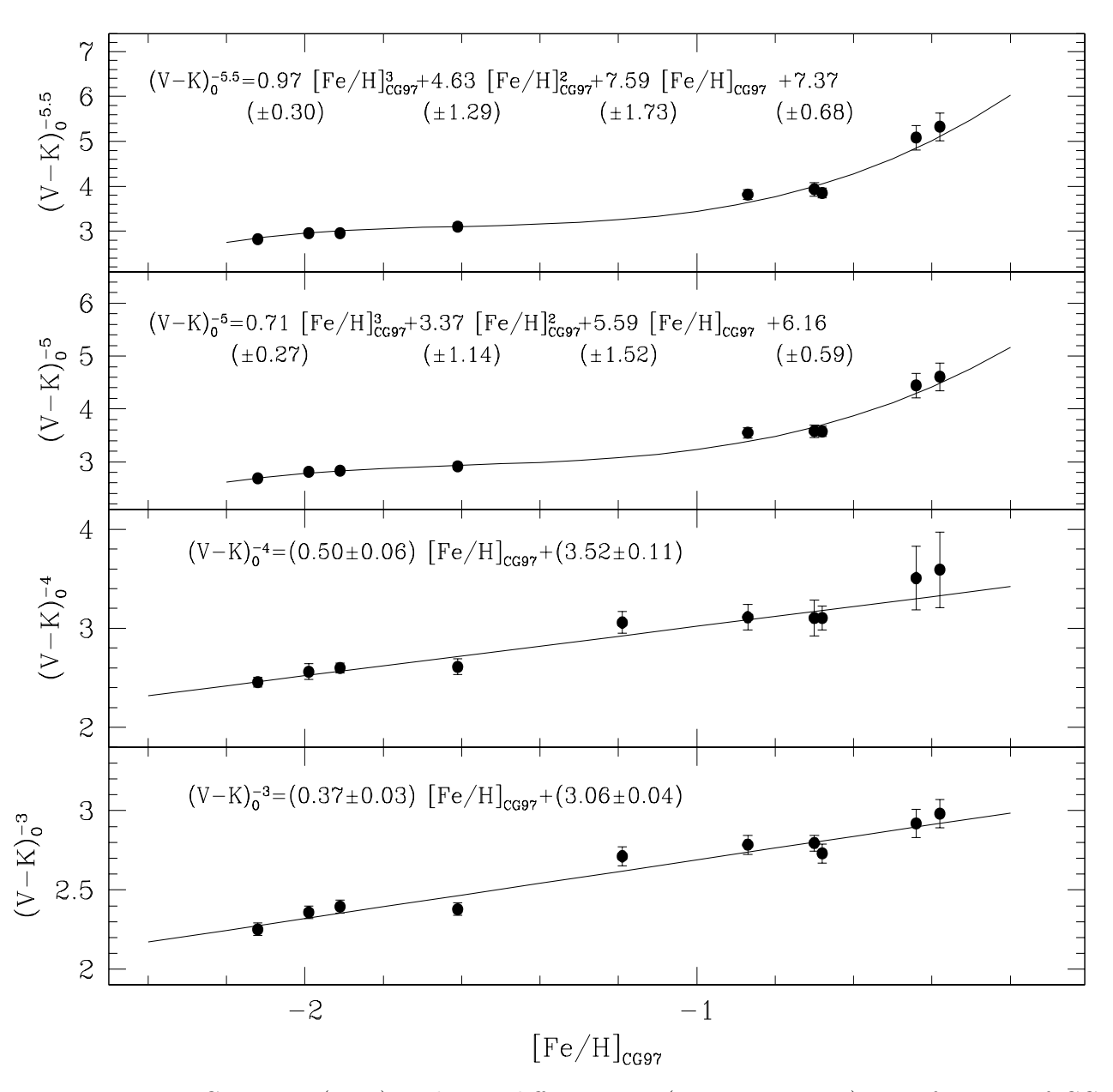


Fig. 6.— RGB mean  $(V-K)_0$  color at different  $M_K$  (-3, -4, -5, -5.5) as a function of CG97 metallicity for the 10 GGCs in our sample.

distance moduli and reddening corrections listed in Table 1 to locate the observed RGB fiducial ridge lines in the absolute  $M_K$ ,  $(J-K)_0$  and  $M_K$ ,  $(V-K)_0$  planes, as plotted in Fig.3.

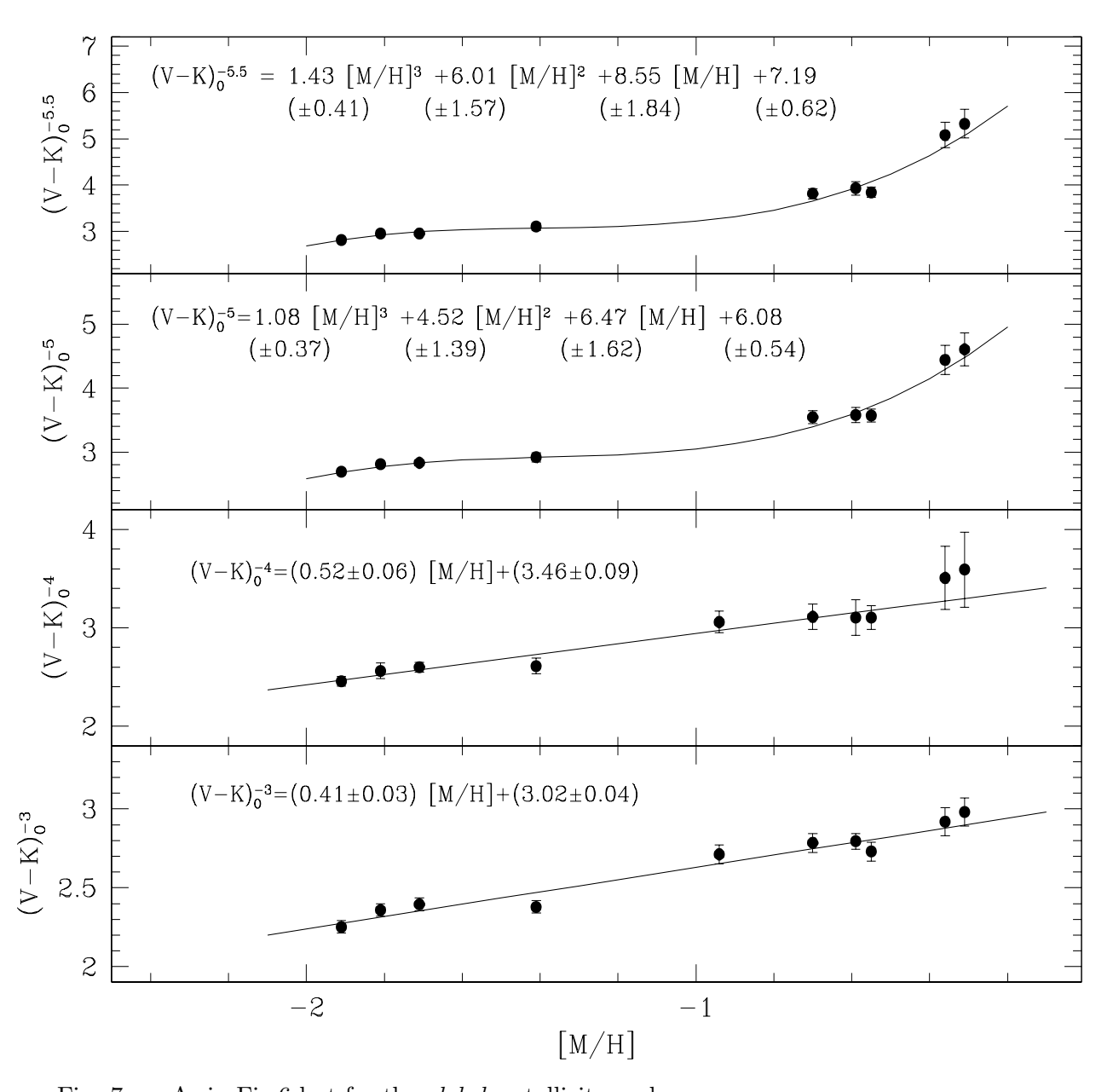


Fig. 7.— As in Fig.6 but for the *global* metallicity scale.

## 6.1. The RGB colors at fixed K magnitudes

The intrinsic  $(J-K)_0$  and  $(V-K)_0$  colors of the RGB measured at different absolute K magnitudes  $(M_K=-3,-4,-5,-5.5, \text{ cf. Sect.5.1})$  for the selected clusters are listed in Table 2 and 3, respectively. In Fig.4–7, we have plotted the RGB  $(J-K)_0$  and  $(V-K)_0$  colors as a function of the adopted cluster metallicity in the CG97  $([Fe/H]_{CG97})$  and the global ([M/H]) scales. The best fit relation to the data is also reported in each panel.

As can be seen from Figure 4 and 5, the RGB (J-K)<sub>0</sub> color scales linearly with [Fe/H], inde-

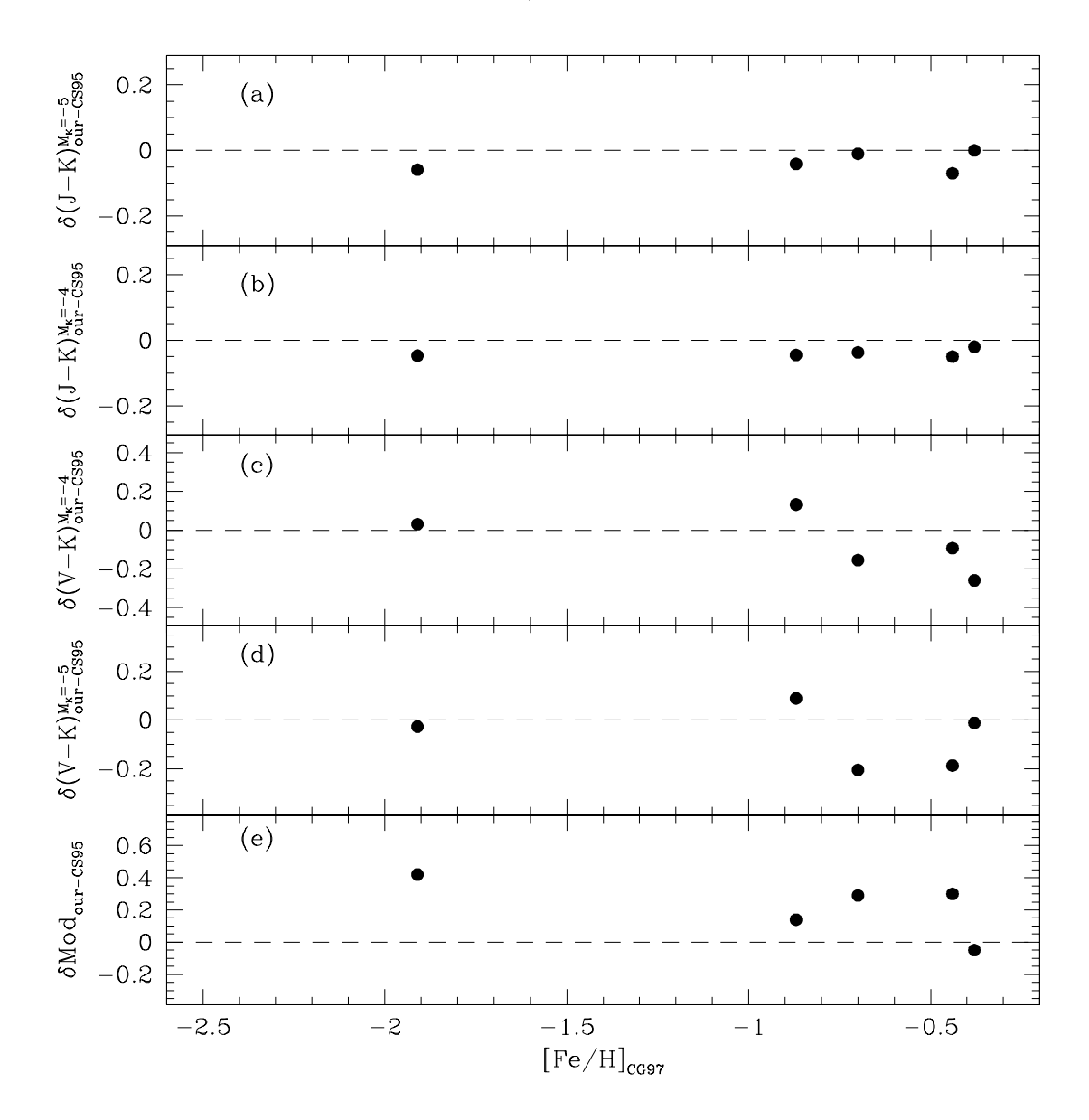


Fig. 8.— Comparison between our and CS95 RGB  $(V-K)_0^{M_K=-5}$ ,  $(V-K)_0^{M_K=-4}$ ,  $(J-K)_0^{M_K=-4}$ ,  $(J-K)_0^{M_K=-5}$  colors for the 5 GGCs in common (panels (a),(b),(c),(d), respectively). In panel (e) we also plotted the difference between the distance moduli adopted here and those adopted by CS95.

pendently of the selected RGB height-cut, and the slope increases progressively towards the RGB tip.

On the other hand, the RGB (V-K)<sub>0</sub> color significantly deviates from a linear dependence at high metallicity (see the upper two panels in Figs.6 and 7). This behavior fully confirms the effect noted by CS95, who found that the  $\Delta$ [Fe/H]/ $\Delta$ (V-K)<sub>0</sub> gradient decreases with increasing [Fe/H].

In order to estimate the possible impact on the inferred color – metallicity relations, by using different samples and different assumptions on the distance scale and reddening, we compare our

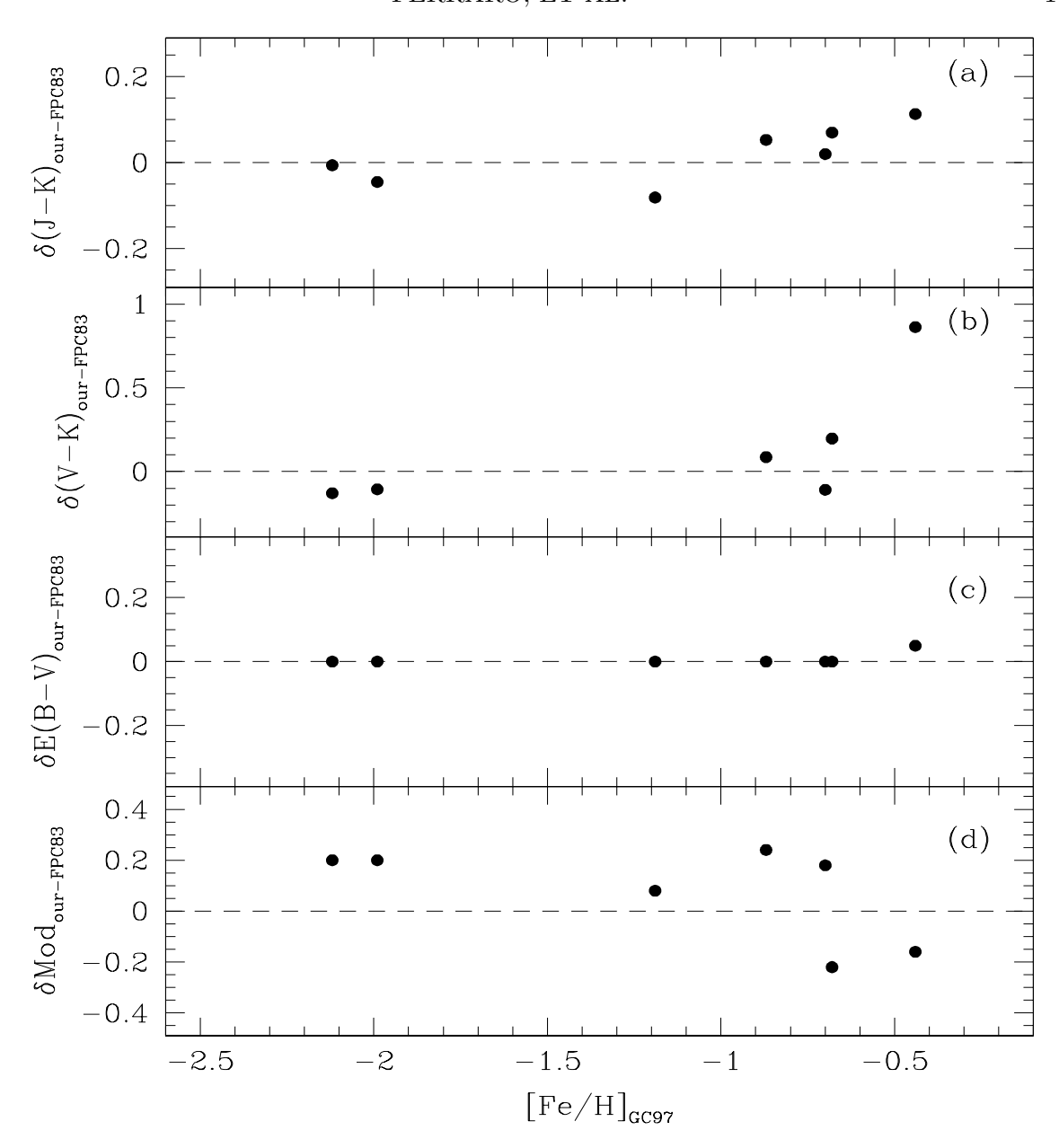


Fig. 9.— Comparison between our and FCP83 RGB  $(V-K)_0^{M_K=-5.5}$  and  $(J-K)_0^{M_K=-5.5}$  colors for the 7 GGCs in common (panels (a),(b), respectively). In panel (c) and (d) we plotted the differences in the adopted reddening and distance moduli, respectively.

results with the two sets of RGB parameters obtained by CS95 and FCP83.

Cluster	[Fe/H]	$(J-K)_0^{-5.5}$	$(J-K)_0^{-5}$	$(J-K)_0^{-4}$	$(J-K)_0^{-3}$
NGC104	-0.70	$1.000 \pm 0.029$	$0.930 \pm 0.026$	$0.813 \pm 0.021$	$0.722 \pm 0.016$
NGC4590	-1.99	$0.725 \pm 0.012$	$0.696 \pm 0.011$	$0.642 \pm 0.010$	$0.594 \pm 0.009$
NGC6121	-1.19	$0.879 \pm 0.017$	$0.836 \pm 0.017$	$0.755 \pm 0.015$	$0.685 \pm 0.013$
NGC6171	-0.87	$0.983 \pm 0.026$	$0.919 \pm 0.025$	$0.805 \pm 0.021$	$0.710 \pm 0.017$
NGC6528	-0.38	$1.101 \pm 0.029$	$1.030 \pm 0.028$	$0.900 \pm 0.024$	$0.786 \pm 0.021$
NGC6553	-0.44	$1.023 \pm 0.023$	$0.960 \pm 0.026$	$0.840 \pm 0.022$	$0.740 \pm 0.018$
NGC6637	-0.68	$0.980 \pm 0.024$	$0.923 \pm 0.022$	$0.819 \pm 0.019$	$0.730 \pm 0.016$
NGC6809	-1.61	$0.749 \pm 0.017$	$0.708 \pm 0.015$	$0.641 \pm 0.012$	$0.590 \pm 0.009$
NGC7078	-2.12	$0.714 \pm 0.014$	$0.680 \pm 0.013$	$0.620 \pm 0.011$	$0.571 \pm 0.009$
NGC7099	-1.91	$0.725 \pm 0.014$	$0.691 \pm 0.013$	$0.633 \pm 0.011$	$0.583 \pm 0.009$

Table 2. Inferred RGB (J-K)<sub>0</sub> colors for the observed GGCs.

Table 3. Inferred RGB (V-K)<sub>0</sub> colors for the observed GGCs.

Cluster	[Fe/H]	$(V-K)_0^{-5.5}$	$(V - K)_0^{-5}$	$(V - K)_0^{-4}$	$(V-K)_0^{-3}$
NGC104	-0.70	$3.93 \pm 0.15$	$3.58 \pm 0.12$	$3.11 \pm 0.18$	$2.80 \pm 0.05$
NGC4590	-1.99	$2.95 \pm 0.06$	$2.81 \pm 0.05$	$2.56 \pm 0.08$	$2.36 \pm 0.04$
NGC6121	-1.19	_	$3.48 \pm 0.09$	$3.06 \pm 0.11$	$2.71 \pm 0.06$
NGC6171	-0.87	$3.82 \pm 0.11$	$3.55 \pm 0.10$	$3.11 \pm 0.13$	$2.78 \pm 0.06$
NGC6528	-0.38	$5.33 \pm 0.31$	$4.61 \pm 0.26$	$3.59 \pm 0.38$	$2.98 \pm 0.09$
NGC6553	-0.44	$5.08 \pm 0.27$	$4.44 \pm 0.23$	$3.51 \pm 0.32$	$2.92 \pm 0.09$
NGC6637	-0.68	$3.85 \pm 0.11$	$3.57 \pm 0.10$	$3.10 \pm 0.12$	$2.73 \pm 0.06$
NGC6809	-1.61	$3.10 \pm 0.08$	$2.92 \pm 0.07$	$2.61 \pm 0.08$	$2.38 \pm 0.04$
NGC7078	-2.12	$2.82 \pm 0.05$	$2.69 \pm 0.05$	$2.46 \pm 0.05$	$2.25 \pm 0.04$
NGC7099	-1.91	$2.96 \pm 0.05$	$2.83 \pm 0.05$	$2.60 \pm 0.05$	$2.39 \pm 0.04$

### 6.1.1. Comparison with CS95

CS95 presented JK photometry of five GGCs (NGC5927, NGC6528, NGC 6624, M107 and M30). They also included in their sample an additional metal rich cluster (NGC6553) observed by Davidge & Simons (1994a) and three reference clusters (47 Tuc, M13 and M92) observed by Cohen et al. (1978) and Frogel et al. (1981). The adopted reddening, metallicity and distance are listed in their Table 10 together with the measured (J–K)<sub>0</sub> and (V–K)<sub>0</sub> colors at  $M_K$ =–4 and  $M_K$ =–5.

Five out of the nine GGCs studied by CS95 (47Tuc, M107, NGC6528, NGC6553 and M30) are in common with our sample. A direct comparison between the  $(J-K)_0$  and  $(V-K)_0$  colors at  $M_K=-4$  and  $M_K=-5$  is then possible. The residuals (this paper – CS95) of the RGB colors as a function of the cluster metallicity are plotted in Fig.8 (panel (a), (b), (c), (d) respectively).

As can be seen, our  $(J-K)_0$  colors seem to be systematically  $\sim 0.05$  mag bluer than the CS95 ones (cf. panels (a) and (b) in Fig.8). We note that the reddenings assumed here are fully consistent

Cluster	[Fe/H]	$M_K^{(J-K)_0=0.7}$	$M_K^{(V-K)_0=3}$	$slope_{RGB}$
NGC 104	-0.70	$-2.71 \pm 0.28$	$-3.70 \pm 0.17$	$-0.104 \pm 0.002$
NGC4590	-1.99	$-5.07 \pm 0.36$	$-5.65 \pm 0.18$	$-0.048 \pm 0.003$
NGC6121	-1.19	$-3.23 \pm 0.31$	$-3.85 \pm 0.37$	$-0.074 \pm 0.009$
NGC6171	-0.87	$-2.88 \pm 0.26$	$-3.69 \pm 0.40$	$-0.101 \pm 0.005$
NGC6528	-0.38	$-2.11 \pm 0.20$	$-3.04 \pm 0.60$	$-0.110 \pm 0.002$
NGC6553	-0.44	$-2.53 \pm 0.25$	$-3.17 \pm 0.57$	$-0.095 \pm 0.002$
NGC6637	-0.68	$-2.59 \pm 0.33$	$-3.75 \pm 0.27$	$-0.092 \pm 0.002$
NGC6809	-1.61	$-4.89 \pm 0.29$	$-5.23 \pm 0.30$	$-0.049 \pm 0.003$
NGC7078	-2.12	$-5.31 \pm 0.30$	$-6.14 \pm 0.31$	$-0.047 \pm 0.001$
NGC7099	-1.91	$-5.13 \pm 0.31$	$-5.66 \pm 0.21$	$-0.043 \pm 0.003$

Table 4. Magnitudes and slopes of the RGB for the observed GGCs.

with those assumed by CS95 (the largest difference being  $\delta E(B-V) \sim 0.06$  mag in the case of NGC6553). On the other hand, the distance moduli assumed in this paper are systematically larger (up to  $\sim 0.4$  mag, cf. panel (e) in Fig.8) than those adopted by CS95.

The slope of the RGB in the  $M_K$ , $(J-K)_0$  plane is  $\sim$ -0.1 in metal-rich clusters and  $\sim$ -0.05 in metal-poor ones (see Sect.6.3), hence a difference of -0.2 in the distance modulus moves the J-K color at a fixed K magnitude by  $\sim$ 0.01-0.02 mag to the red. Thus, if we assume the same distance scale as CS95, the discrepancy is reduced to  $\leq$ 0.02 mag, that is well within the level of accuracy of both photometries.

In summary, the observed discrepancy between our and CS95  $(J-K)_0$  colors can be mainly ascribed to differences in the assumed distance moduli, while the reddening and zero–point photometric calibrations are in reasonable agreement.

Moving to the  $(M_K,(V-K)_0)$  plane, the discrepancy between our  $(V-K)_0$  colors and those presented by CS95 (cf. panels (c) and (d) in Fig.8) are remarkably larger (up to about -0.35 mag). Two main factors can be invoked to explain such a discrepancy.

Different assumptions in the distance moduli produce a variation in the V–K color which is strongly dependent on the metallicity, due to the corresponding strong dependence of the RGB slope on the metallicity itself. Since we assumed larger distance moduli than CS95, we expect to derive (V–K)<sub>0</sub> colors systematically bluer than CS95, with progressively larger differences at larger metallicity, as indeed observed.

Different calibrations of the zero–point in the V magnitude also directly affect the (V–K)<sub>0</sub> color. CS95 used old V photometry for NGC6553 (Hartwick 1975), NGC6528 ( Van Den Berg & Younger 1979) and NGC6171 (Sandage & Katem 1964). While the photometry of NGC6171 by Sandage & Katem (1964) is consistent with the one adopted here (Ferraro et al. 1991), systematic differences are present in the case of NGC6553 and NGC6528.

#### 6.1.2. Comparison with FCP83

FCP83 presented RGB parameters for 33 GGCs. 7 out of 10 GGCs presented in this paper are in common with FCP83 (47Tuc, M68, M4, M107, M69, M15 and NGC6553).

The residuals (this paper – FCP83) for the  $(J-K)_0^{-5.5}$  and  $(V-K)_0^{-5.5}$  colors as a function of metallicity are plotted in Fig.9 (panel (a) and (b), respectively). From inspecting this figure a possible trend of the  $(J-K)_0$  and  $(V-K)_0$  color residuals as a function of the metallicity is present (cf. panels (a) and (b)), even though based on a poor statistics to draw any firm conclusions.

Our photometry tends to be bluer in the metal–poor domain and redder in the metal–rich one. While the adopted reddening corrections are almost identical, (cf. panel (c) in Fig.9), it is interesting to note that, while the distance moduli adopted here are systematically (0.2 mag) larger than those assumed by FCP83, accounting for possible bluer colors at a fixed absolute magnitude, the two most metal rich clusters among those in common (namely, NGC6553 and M69) seem to have distance moduli significantly smaller than those assumed by FCP83 (cf. panel (d) in Fig.9). This fact naturally moves the colors at a fixed magnitude further to the red, and it is especially effective in the upper part of the RGB of metal–rich clusters, for which small variations in magnitude produce a large variation in color (cf. Fig.3).

Moreover, as discussed in the previous section, the V photometry zero–point directly affects the (V-K) color and thus the different optical photometry adopted here with respect to FCP83 is expected to produce significant differences especially in the (V-K) color. In the case of M69, for example, Ferraro et al. (1994a) showed that the B,V photometry by Hartwick & Sandage (1968) and Harris (1977) (adopted by FCP83) has large (up to  $\sim 0.3$  mag) systematic errors.

#### 6.2. The RGB K magnitudes at fixed colors

Following FCP83, we measured, from Fig. 3, the K magnitude  $M_K^{(V-K)_0=3}$  at a fixed  $(V-K)_0=3$  color. In Fig.10 we show the dependence of this parameter on metallicity ( $[Fe/H]_{CG97}$  in panel (a) and [M/H] in panel (b), respectively). The best fit relation is also reported in each panel and plotted as a solid line.

It is worth considering that our linear square fitting turns out to be significantly steeper (1.63 and 1.73 using  $[Fe/H]_{CG97}$  and [M/H], respectively) than the FCP83 relation (plotted as a dashed line in panel (a) of Fig.10). Part of this discrepancy can be ascribed to the adopted metallicity scale. Using the Zinn scale as FCP83 did, we would in fact obtain a shallower slope (1.43) than using CG97 metallicity scale, but still steeper than the FCP83 one ( $\sim 1.1$ ).

In the same vein as for  $M_K^{(V-K)_0=3}$ , we have defined a similar parameter in the  $M_K$ ,  $(J-K)_0$  plane, namely  $M_K^{(J-K)_0=0.7}$ , the absolute K magnitude at fixed  $(J-K)_0=0.7$  color. This new parameter allows to characterize the RGB from a merely IR CMD and to constrain the photometric estimate of metallicity and reddening of obscured stellar clusters.

The behavior of this new parameter as a function of metallicity ( $[Fe/H]_{CG97}$  in panel (a) and [M/H] in panel (b), respectively) is shown in Fig.11. The best fit solutions are also reported. As can be seen from the figures, linear relations nicely match the data.

The inferred absolute K magnitude  $M_K$  at fixed  $(J-K)_0=0.7$  and  $(V-K)_0=3$  RGB colors of the

selected clusters are listed in columns 3 and 4 of Table 4, respectively.

The uncertainties in the derived RGB K magnitude are essentially driven by the errors in the reddening. As expected, errors of a few hundredths of magnitude produce uncertainties of  $\sim 0.2-0.3$  mag in the K magnitudes, depending on the RGB region intercepted (see Figure 3). Significative higher errors are only inferred for the two most metal-rich clusters (NGC6553 and NGC6528) due to their very uncertain reddening estimates.

## 6.3. The RGB slopes

To further describe the RGB properties in the IR CMD, we have also measured the so-called RGB slope ( $slope_{RGB}$ ), adopting the technique used by K95 and KF95. Even though linear fits are not the best tools to represent the upper RGB (also in the (K,J-K) plane), they can be used as a first-order description of the overall RGB morphology.

A basic step before measuring the slope is to isolate the RGB stars from field objects and members of different branches. This is not an easy task and we used the RGB samples here selected as described in Sect.3, where the AGB and HB stars have been *statistically* removed from the CMD, before performing the linear fit to the data.

The derived slopes for the 10 GGCs in our sample are listed in column 5 of Table 4. From the examination of these values it is evident how the RGB slope is a sensitive indicator of the cluster metal content: the average slope for the 5 most metal rich clusters in our sample (with  $[Fe/H]_{CG97} > -1$ ) turns out to be  $< slope_{RGB} > = -0.1004 \pm 0.007$ , while it is significantly flatter ( $< slope_{RGB} > = -0.047 \pm 0.003$ ) in the 4 most metal poor ones with  $[Fe/H]_{CG97} < -1.5$ . This result fully confirms the KF95 suggestion that the RGB slope in the K,J–K plane is indeed one of the most robust (reddening–independent) indicator of the cluster metallicity.

Fig.12 shows a linear correlation of the RGB slope with the metallicity ( $[Fe/H]_{CG97}$  in panel (a) and [M/H] in panel (b), respectively). The inferred relations (also reported in Fig.12) are fully compatible with those by K95 and KF95. Small differences can be ascribed both to the different metallicity scale adopted here (CG97 rather than Z85 used by K95 and KF95), and to the fact that their relations have been derived only for metal rich clusters ([Fe/H] > -1), while those reported in Fig.12 have been derived including also metal—poor ones. Two GGCs are in common between our and the K95–KF95 samples, namely 47Tuc and M69. These clusters allow us to perform a direct comparison. In the case of 47 Tuc slightly different slopes have been measured: we get  $slope_{RGB} = -0.104$  while K95 found -0.097. In the case of M69 the values are fully in agreement: we infer  $slope_{RGB} = -0.092$  compared to -0.093 by K95. However, we note that the quality (both in terms of photometric accuracy and sample size) of the IR CMDs presented here for 47 Tuc and for the other cluster is superior to the K95 data—base (compare, for example, the diagrams in Fig.1 with the last two panels of Figure 11 in K95).

#### 6.4. The RGB bump

One of the most interesting features along the RGB is the so-called RGB bump (Iben 1968). Its name is due to the peaked distribution of the differential luminosity function along the RGB.

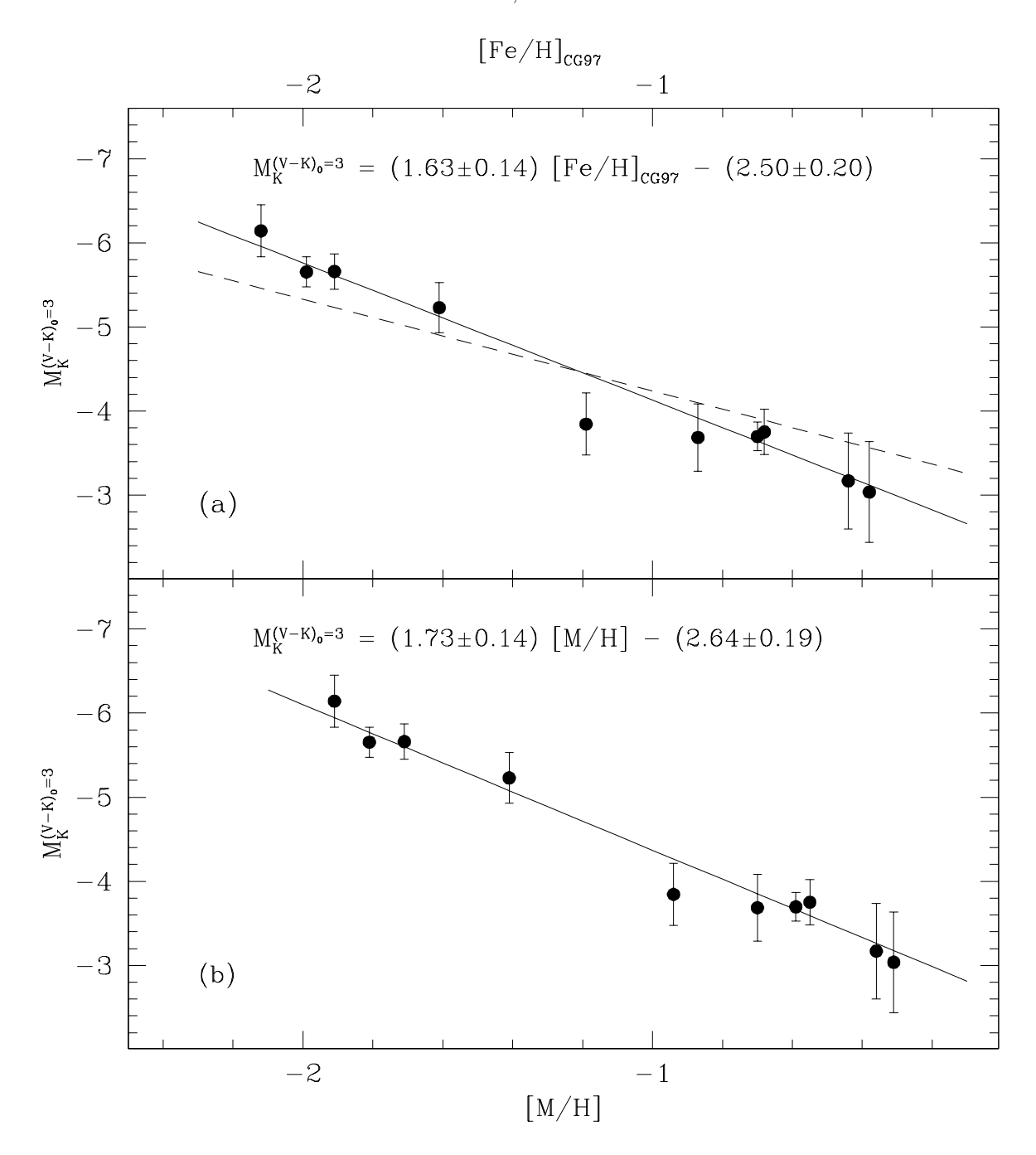


Fig. 10.—  $M_K$  at constant  $(V-K)_0=3$  as a function of the metallicity in the CG97 (panel (a)) and in the global scale (panel(b)), respectively, for the 10 GGCs in our sample. The solid lines are the best fit to the data, the dashed line is the FCP83 relation.

The RGB evolution is characterized by a narrow burning hydrogen shell which is moving towards the outer region of the star. The shell is quite thin in mass and a temporary drop in luminosity is expected when it reaches the discontinuity in the hydrogen distribution profile gen-

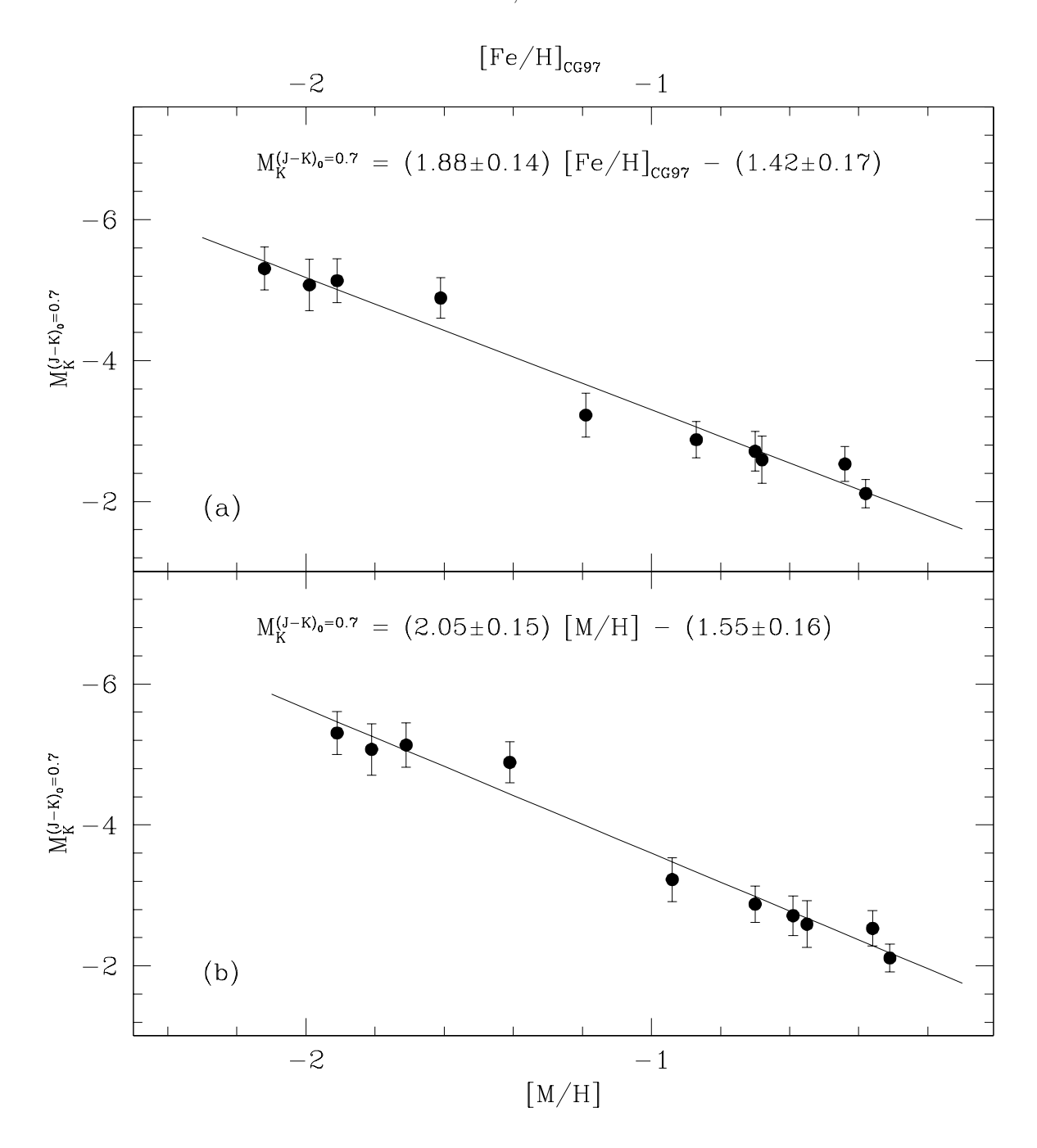


Fig. 11.—  $M_K$  at constant  $(J-K)_0=0.7$  as a function of the metallicity in the CG97 (panel (a)) and in the global scale (panel(b)), respectively, for the 10 GGCs in our sample. The solid lines are the best fit to the data.

erated by the inner penetration of the convective envelope. This interruption in the expansion of the stellar envelope has its signature in the differential LF star excess, the so-called bump.

Fusi Pecci et al. (1990) and recently F99 showed how this feature can be safely identified in

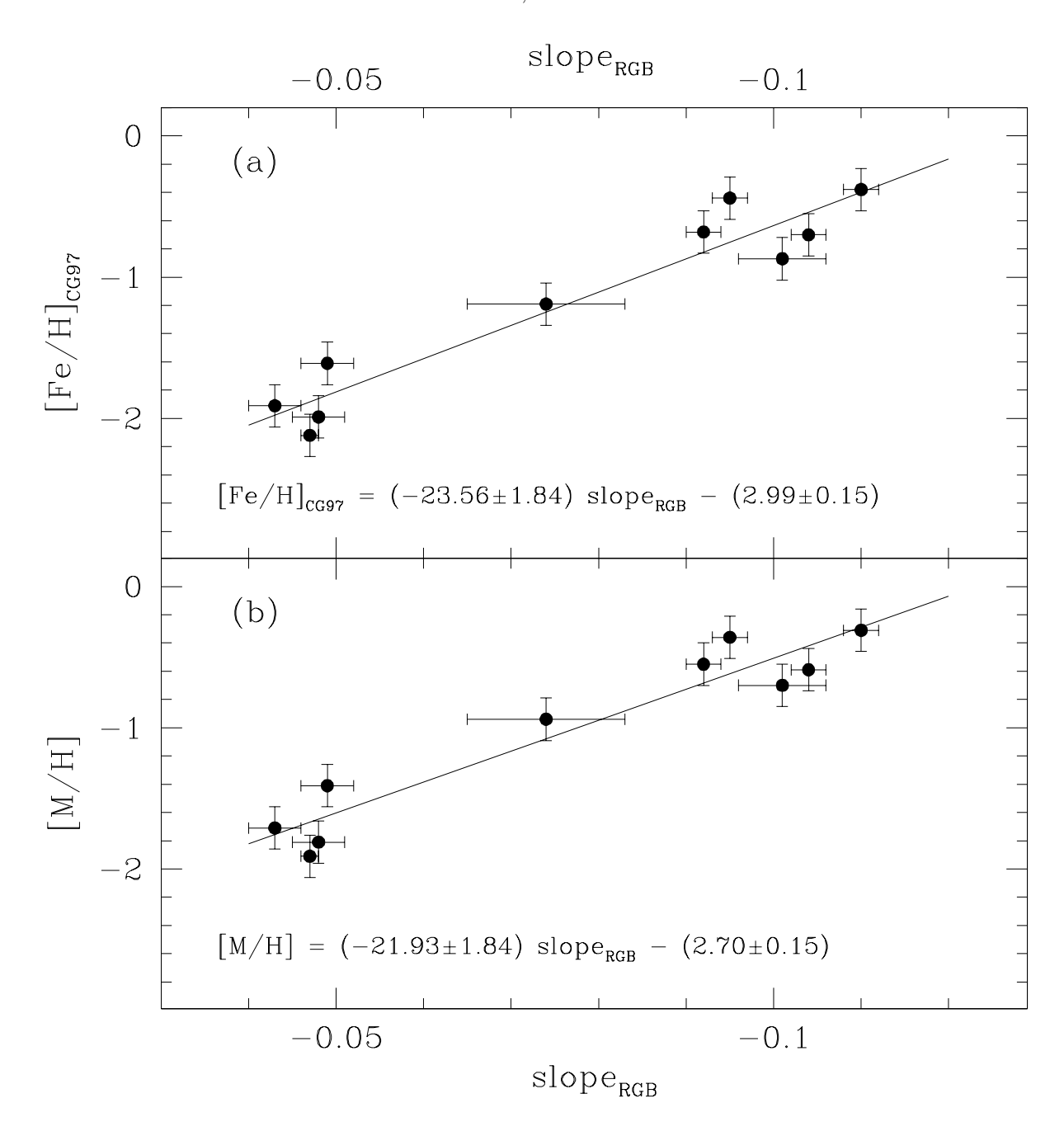


Fig. 12.— Metallicity scales:  $[Fe/H]_{CG97}$  and [M/H], (panel(a) and panel (b), respectively) as a function of the derived RGB slope for the 10 selected GGCs.

most of the current generation of optical CMDs. As already noted by Crocker & Rood (1984) and Fusi Pecci et al. (1990), the main difficulty in detecting the RGB bump is having sufficiently large observational samples (about 2000 RGB stars in the upper 3 mag). Moreover, since in metal—poor clusters the RGB bump occurs at brighter luminosities, that is in a region which is intrinsically

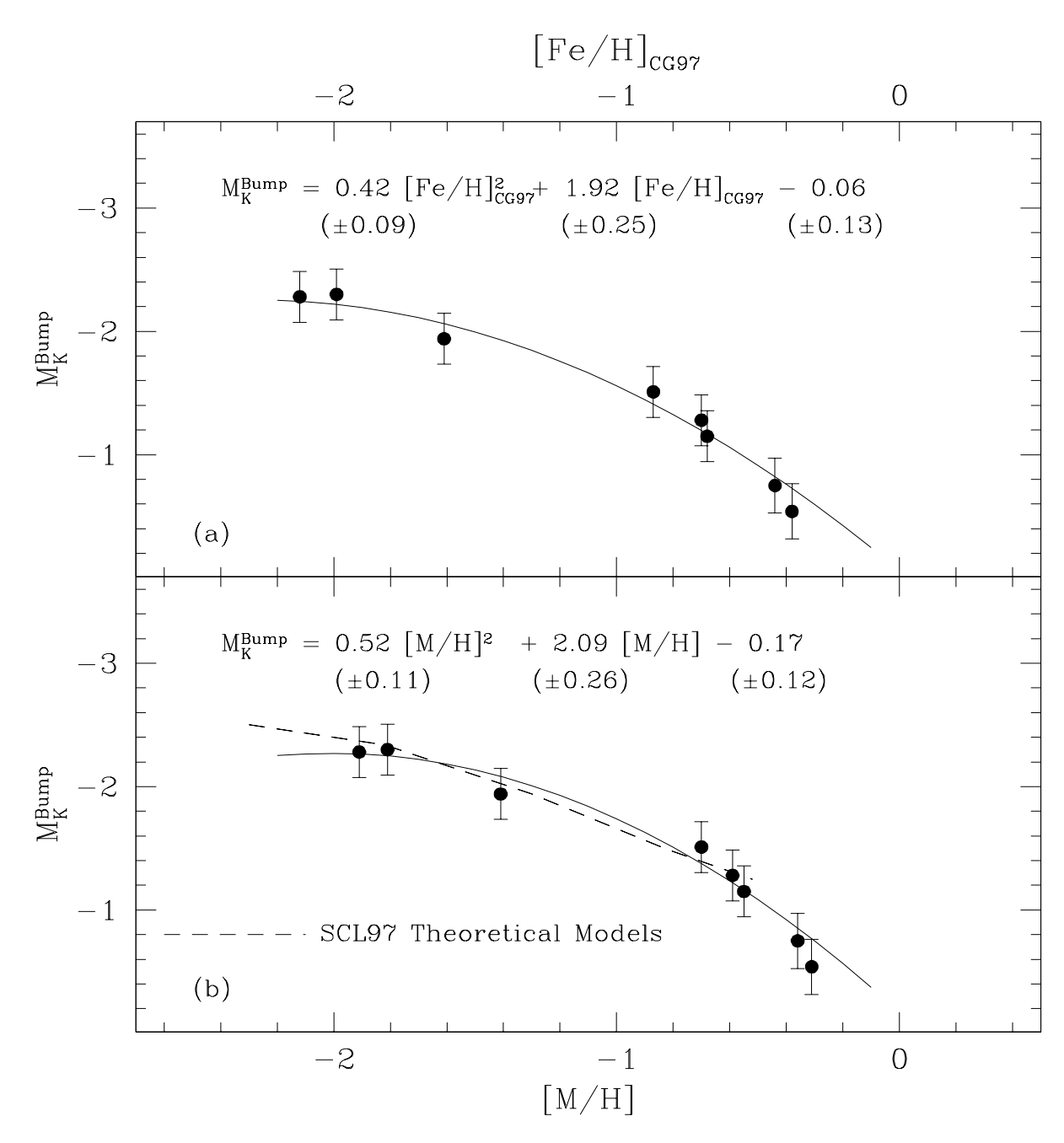


Fig. 13.— Absolute K magnitude at the RGB bump as a function of the metallicity (in the CG97 and global metallicity scales – panel(a) and (b), respectively), for the 8 GGCs in our sample, in which the RGB-bump has been identified. The solid lines are the best fit to the data. The dashed line in panel(b) is the theoretical prediction by SCL97 models at t = 16 Gyr.

poorly populated (towards the upper RGB), its identification is even more difficult.

Following Fusi Pecci et al. (1990) we used the integral and differential LFs to correctly locate the bump. In all but two clusters, namely M4 and M30, we succeeded in identifying the RGB bump

with good accuracy. This is so far the largest near IR sample of Population II stars ever observed for which it is possible to measure the RGB bump. The observed  $K^{Bump}$  magnitude, the absolute magnitude  $M_K^{Bump}$  and the  $(J-K)_0$  and  $(V-K)_0$  colors of the RGB bump for the selected clusters are listed in Table 5. As can be seen, the size of the IR samples presented here allows a very accurate determination of this feature, similar to that one typically obtained from optical CMDs (cf. e.g. Table 5 in F99).

In Fig.13 the absolute K magnitude of the RGB bump as a function of the cluster metallicity in both scales ( $[Fe/H]_{CG97}$  and [M/H]) is plotted. The best fit relation to the data is also plotted as a solid line and the equation reported in each panel. As already noted in Sect.4.3, the errors in the determinations of the absolute K magnitudes are mainly driven by the uncertainties in the distance moduli.

The dashed line in panel (b) of Fig.13 represents the theoretical expectations based on the SCL97 models, for an age of t=16 Gyr (Straniero 1999, private communication). As can be seen, the models show an excellent agreement with the observational data. This result fully confirms the finding of F99 (from the location of the RGB bump in 47 GGCs in the visual band) that the earlier discrepancy between theory and observations ( $\sim 0.4$ mag) (cf. Fusi Pecci et al. 1990, Ferraro 1992) has been completely removed using the latest theoretical models and the global metallicity ([M/H]).

# 6.5. The RGB tip

A quite well defined relationship between the bolometric luminosity of the brightest RGB star in a GGC and its metallicity has been found by Frogel, Persson & Cohen (1981) and FCP83. This finding had a noteworthy impact both on testing the theoretical models and on the use of the brightest TGB stars as possible distance indicators.

In order to derive a similar relation using our sample of GGCs, we identified the *candidate* brightest giant in each cluster, paying particular care in the decontamination of possible field objects and (especially in the case of metal—rich clusters) of bright AGB stars and the variables commonly associated to the AGB, the so—called Long Period Variables (LPV). Of course, the degree of reliability of the decontamination is hard to quantify due to the very small number of stars populating the brightest extreme of the giant branch, possibly affected by severe statistical fluctuations.

Table 6 reports the absolute K and bolometric magnitudes of the adopted brightest star (the observed RGB tip) for 9 of the 10 clusters considered in this paper (M4 was excluded since the number of sampled giants is too low). Fig.14 shows the absolute K magnitude of the tip as a function of the metallicity in the CG97 and global scales (panel (a) and (b)), respectively.

The following best fit relations have been derived:

$$M_K^{Tip} = -(0.59 \pm 0.11)[Fe/H]_{CG97} - (6.97 \pm 0.15)$$
  
 $M_K^{Tip} = -(0.64 \pm 0.12)[M/H] - (6.93 \pm 0.14)$ 

and they are plotted as solid lines in panel (a) and (b) of Figure 14, respectively. Two points have been plotted for NGC6528. This is a very metal-rich cluster and, like for instance 47 Tuc, it is

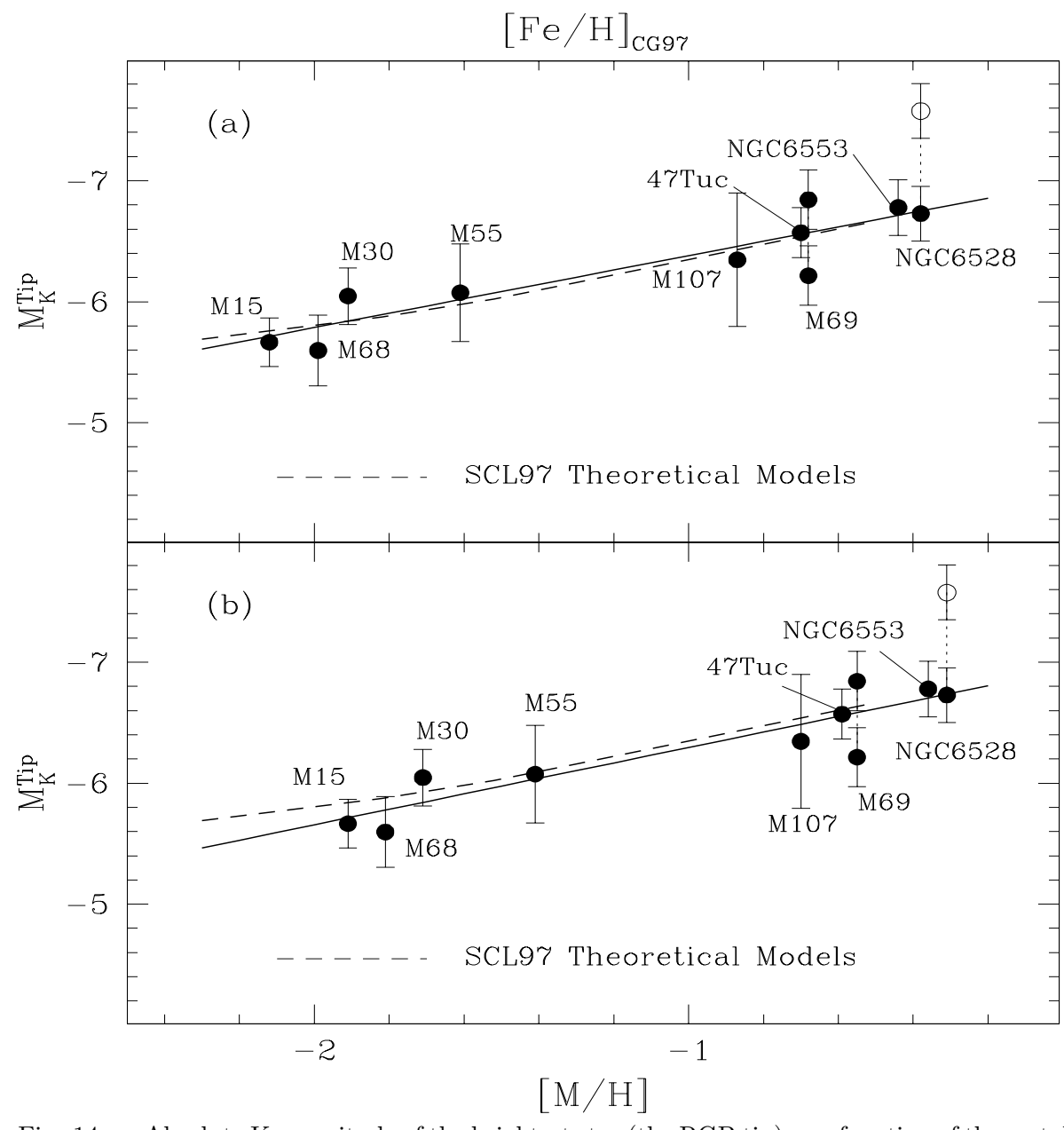


Fig. 14.— Absolute K magnitude of the brightest star (the RGB tip) as a function of the metallicity in the CG97 and global scale -panel(a) and (b), respectively - for the GGCs in our sample. Two points have been plotted for NGC6528 and M69 (cf. Sect.6.5 for discussion). Stars belonging to the same cluster are connected by dotted lines. The solid lines are the best fit to the data, the dashed lines are the theoretical expectations based on SCL97 models at t=16 Gyr.

expected to have a number of bright variable AGB stars, populating the upper part of the RGB. These stars have not been identified in this cluster yet, so a clear discrimination is not possible. For this reason we have plotted the brightest star in our sample as an empty circle, but since it could

possibly be a LPV, we also consider as *candidate* brightest RGB (*non variable*) star the reddest star among the brightest 5 stars in our photometry (filled circle in Fig.14).

The case of M69 is also worth of a brief discussion since the brightest not variable star in our photometry is star #785 (cf. Figure 13 by Ferraro et al. 1994a). However, this star seems too blue in the (K,V–K) CMD to be a real RGB star (cf. panel (b) of Figure 13 in Ferraro et al. 1994a). For this reason in this cluster we also consider the second brightest star (namely #399). Both these stars have been reported in Table 5 and in Fig.14.

Finally, the dashed line plotted in Fig.14 represents the theoretical expectation based on SCL97 models at t=16 Gyr (Straniero 1999, private communication). As can be seen the theoretical prediction nicely agrees with the observations and, though residual contamination and statistical fluctuations could still affect the sample, it seems quite rewarding the success of the theory in reproducing the data. It may also be interesting to note that such an agreement indirectly implies that the adopted distances and reddening should not be affected by large errors.

Cluster	[Fe/H]	$K^{Bump}$	$M_K^{Bump}$	$(J-K)_0^{Bump}$	$(V-K)_0^{Bump}$	$M_{Bol}^{Bump}$	$Log(T_e^{Bump})$
NGC 104	-0.70	$12.05 \pm 0.05$	$-1.28 \pm 0.21$	$0.61 \pm 0.01$	$2.41 \pm 0.04$	$0.78 \pm 0.21$	3.6651
NGC4590	-1.99	$12.85 \pm 0.05$	$-2.30 \pm 0.21$	$0.56 \pm 0.01$	$2.24 \pm 0.03$	$-0.42 \pm 0.21$	3.6917
NGC6121	-1.19	_	_	_	_	_	-
NGC6171	-0.87	$12.55 \pm 0.05$	$-1.51 \pm 0.21$	$0.60 \pm 0.01$	$2.44 \pm 0.04$	$0.53 \pm 0.21$	3.6677
NGC6528	-0.38	$14.05\pm0.10$	$-0.54 \pm 0.22$	$0.58 \pm 0.01$	$2.30 \pm 0.04$	$1.45 \pm 0.22$	3.6751
NGC6553	-0.44	$13.00 \pm 0.10$	$-0.75\pm0.22$	$0.59 \pm 0.01$	$2.33 \pm 0.03$	$1.26 \pm 0.22$	3.6722
NGC6637	-0.68	$13.55 \pm 0.05$	$-1.15 \pm 0.21$	$0.62 \pm 0.01$	$2.29 \pm 0.03$	$0.92 \pm 0.21$	3.6645
NGC6809	-1.61	$11.90 \pm 0.05$	$-1.94 \pm 0.21$	$0.55 \pm 0.01$	$2.19 \pm 0.03$	$-0.10 \pm 0.21$	3.6980
NGC7078	-2.12	$12.90 \pm 0.05$	$-2.28 \pm 0.21$	$0.54 \pm 0.01$	$2.13 \pm 0.03$	$-0.45 \pm 0.21$	3.6998
NGC7099	-1.91	-	_	_	_	_	-

Table 5. Inferred RGB bump for the observed GGCs.

### 7. The theoretical plane

The transformations of the observed colors and magnitudes of the RGB features in the theoretical plane have been performed using the bolometric corrections and temperature scales for Population II giants computed and adopted by Montegriffo et al. (1998) (cf. their Table 2).

Since our JK photometry is homogeneous, while the V photometry has been taken from different data sets (including HST observations), the transformations to bolometric magnitudes and effective temperatures were made in the  $M_K$ ,  $(J-K)_0$  rather than in  $M_K$ ,  $(V-K)_0$  plane.

In Fig.15 the fiducial RGB ridge lines for the 10 GGCs in our sample are plotted in the  $M_{Bol}$  vs  $T_e$  theoretical plane. From this CMD we can easily derive the RGB effective temperature at a fixed bolometric magnitude. In Fig.16 the effective temperature at  $M_{Bol}$ =-3 is shown as a function of the metallicity. In particular, adopting the CG97 metallicity scale, we found the following relation

Cluster	[Fe/H]	$(m-M)_0$	$M_K^{Tip}$	$M_{Bol}^{Tip}$
NGC 104	-0.70	13.32	$-6.57 \pm 0.20$	$-3.64 \pm 0.20$
NGC 4590	-1.99	15.14	$-5.60 \pm 0.26$	$-3.29 \pm 0.26$
NGC 6171	-0.87	13.95	$-6.35 \pm 0.43$	$-3.52 \pm 0.43$
NGC6528	-0.38	14.37	$-6.73 \pm 0.22$	$-3.68 \pm 0.22$
NGC6553	-0.44	13.46	$-6.78 \pm 0.22$	$-3.81 \pm 0.22$
NGC 6637	-0.68	14.64	$-6.84 \pm 0.23$	$-3.91 \pm 0.23$
NGC 6637	-0.68	14.64	$-6.21 \pm 0.23$	$-3.44 \pm 0.23$
NGC 6809	-1.61	13.82	$-6.07 \pm 0.33$	$-3.59 \pm 0.33$
NGC 7078	-2.12	15.15	$-5.67 \pm 0.20$	$-3.36 \pm 0.20$
NGC 7099	-1.91	14.71	$-6.05 \pm 0.22$	$-3.80 \pm 0.22$

Table 6. The RGB tip for the observed GGCs.

(cf. panel (a) in Fig.16):

$$LogT_e = -(0.061 \pm 0.003)[Fe/H]_{CG97} + (3.519 \pm 0.005)$$

If the *global* metallicity is adopted, the relation turns out to be slightly different:

$$LogT_e = -(0.064 \pm 0.003)[M/H] + (3.527 \pm 0.005)$$

The formal uncertainties for the derived effective temperatures turn to be  $\sim 50 - 100^{\circ} K$ .

The inferred relations are steeper than in FCP83 (the most metal–poor clusters being hotter and the most metal–rich ones cooler than in FCP83). This effect can be mainly ascribed to the different metallicity scales adopted here, as in the case of the the absolute K magnitude (cf. Fig.8). In fact, using the Zinn's metallicity scale we find a shallower relation:

$$LogT_e = -(0.054 \pm 0.003)[Fe/H]_{Z85} + (3.526 \pm 0.005)$$

very similar to the FCP83 one (cf. dashed line in panel (b) of Fig.16).

In Fig.17 we plotted the bolometric magnitude (panel (a)) and the effective temperature (panel (b)) of the RGB bump as a function of metallicity. In panel (a), a quadratic relation has been derived to describe the bolometric magnitude of the RGB-bump as a function of GC97 metallicity. The corresponding relation using the global metallicity turns to be:

$$M_{Bol}^{Bump} = (0.64 \pm 0.37)[M/H]^2 + (2.53 \pm 0.85)[M/H] + (2.10 \pm 0.35)$$

In panel (b), the effective temperature is plotted as a function of GC97 metallicity and the best fit relation is reported. If the global metallicity ([M/H]) is adopted, we get the following relation:

$$LogT_e = -(0.020 \pm 0.002)[M/H] + (3.660 \pm 0.002)$$

Finally, Fig.18 reports the bolometric magnitude of the RGB-tip for the selected clusters as determined in the previous section. The best fit relations to our data are:

$$M_{Bol}^{Tip} = -(0.25 \pm 0.11)[Fe/H]_{CG97} - (3.96 \pm 0.13)$$

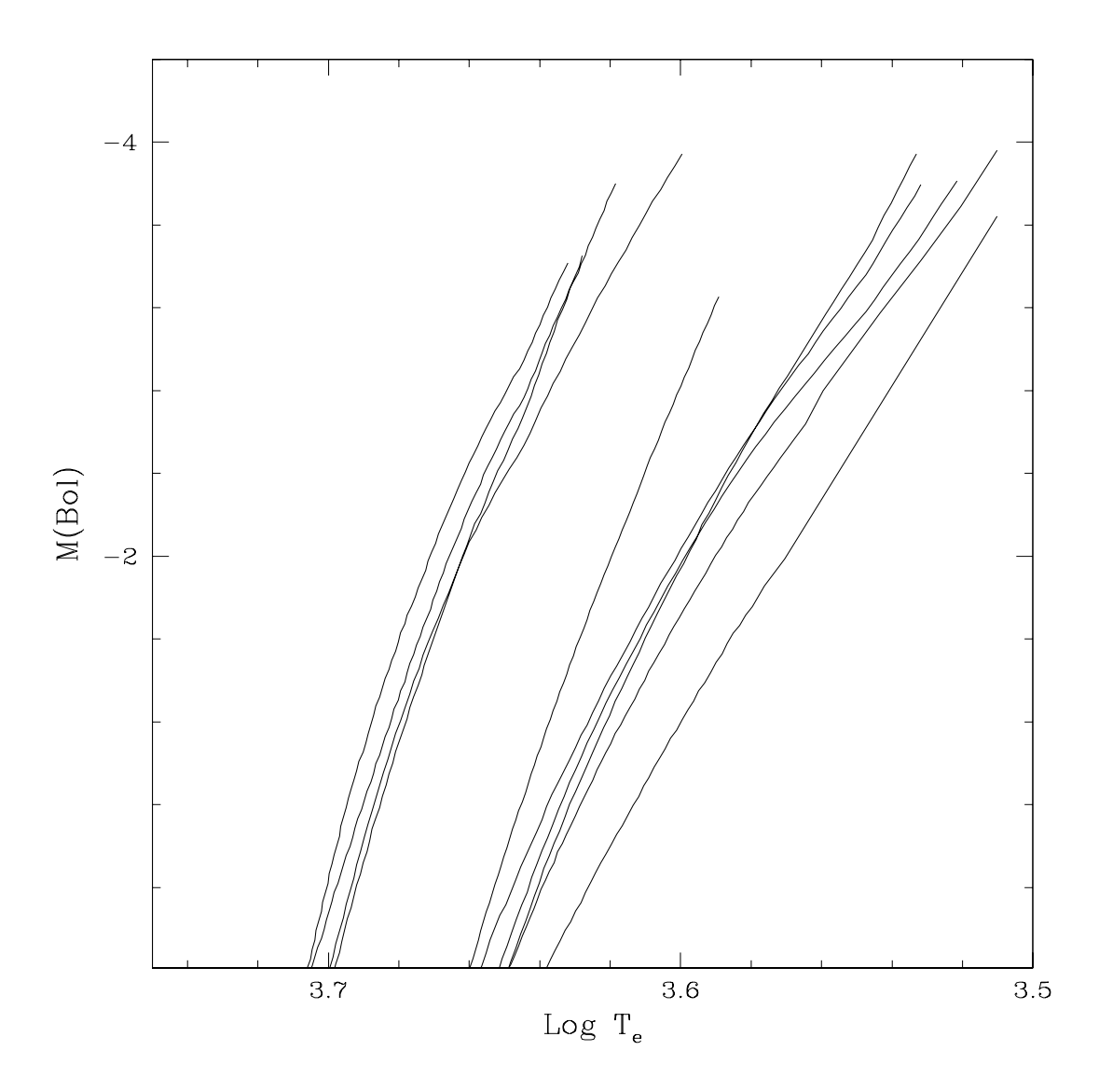


Fig. 15.— RGB fiducial ridge lines in the  $(M_{Bol}, Log(T_e))$  theoretical plane for the 10 GGCs in our sample.

 $\quad \text{and} \quad$ 

$$M_{Bol}^{Tip} = -(0.27 \pm 0.12)[M/H] - (3.94 \pm 0.13)$$

adopting the two metallicity scales, respectively. As can be seen, our result is fully consistent with

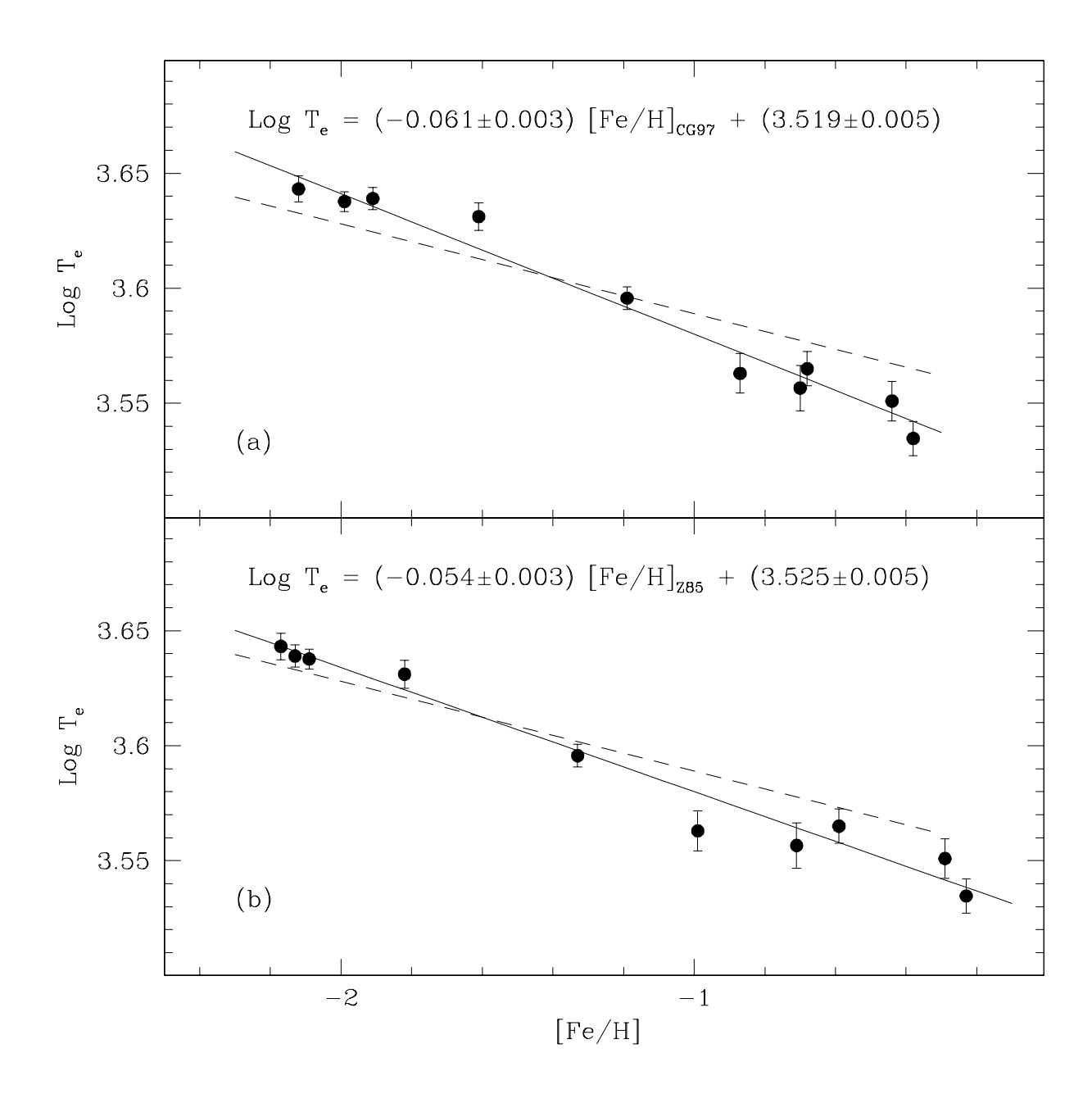


Fig. 16.— Log  $T_e$  at  $M_{Bol}$ =–3 as a function of the metallicity (in the CG97 and Z85 scales - panel(a) and (b), respectively) for the 10 GGCs in our sample. The solid lines are the best fit to the data. The dashed line is the relation by FCP83.

the one obtained by FPC83 (plotted as dashed line in Figure 18):

$$M_{Bol}^{Tip} = -0.26[Fe/H]_{CG97} - 3.82$$

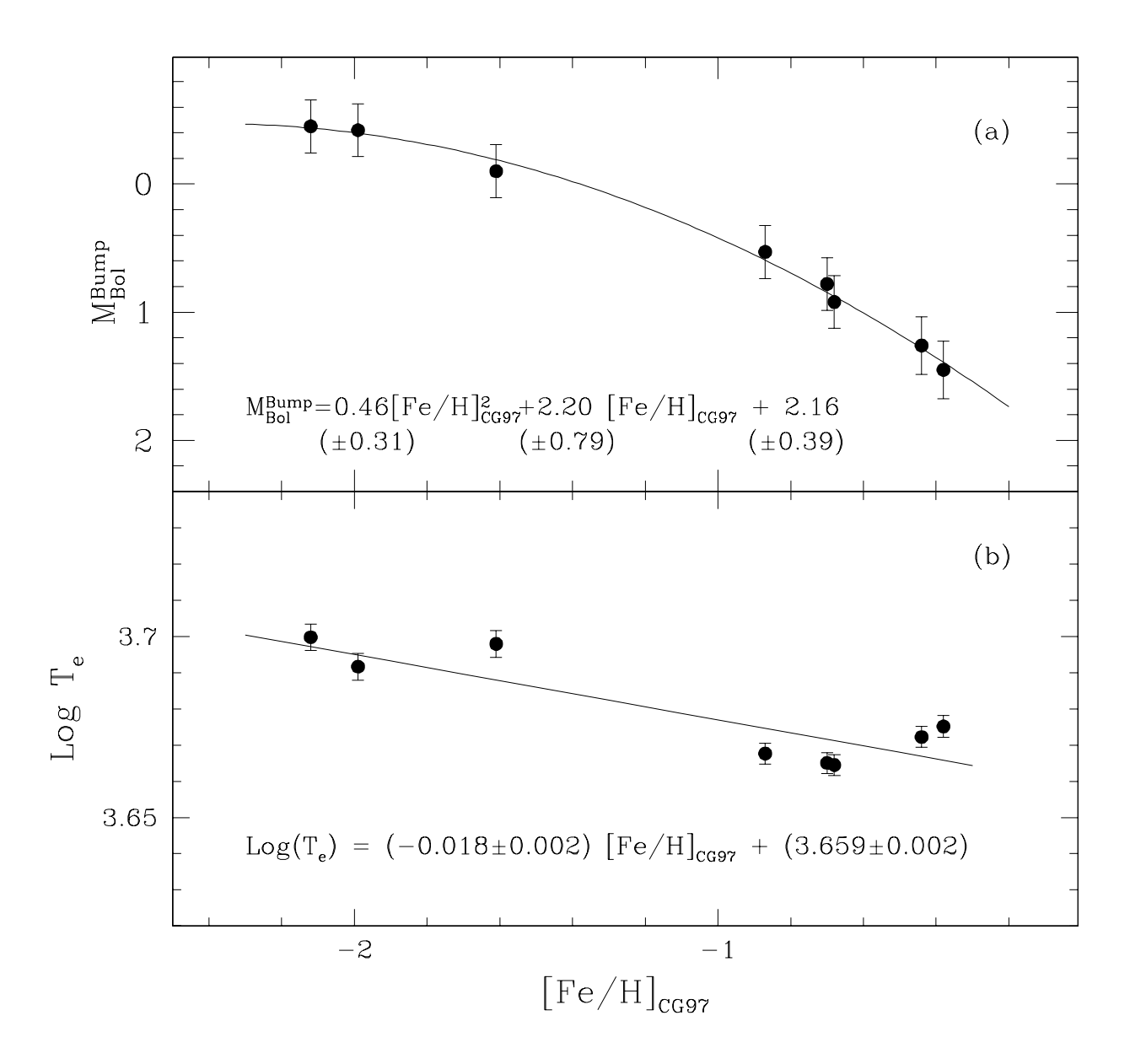


Fig. 17.— Log  $T_e$  (bottom panel) and  $M_{Bol}$  (upper panel) at the RGB bump as a function of the CG97 metallicity scale for 8 GGCs in our sample.

However, it is worthy of noticing that shallower relations are obtained if the brightest RGB star in NGC6528 (plotted as an open circle in Figure 18) is not considered in the fit:

$$M_{Bol}^{Tip} = -(0.15 \pm 0.11) [Fe/H]_{CG97} - (3.79 \pm 0.15)$$

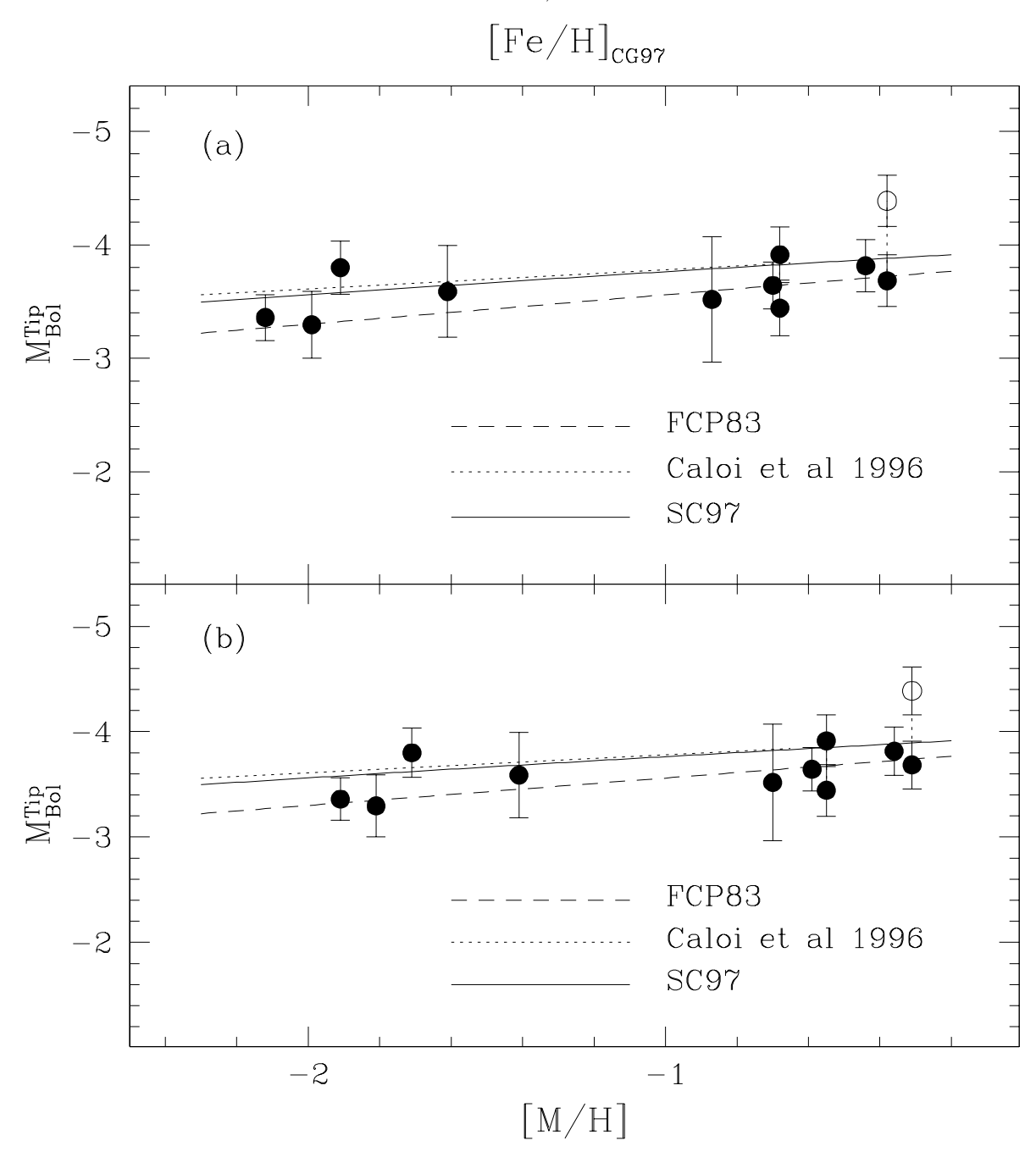


Fig. 18.—  $M_{Bol}$  of the RGB tip as a function of metallicity (in the CG97 and global scale – panel(a) and (b), respectively) for 9 GGCs in our sample. The dashed line is the relation by FPC83. Two theoretical relations have been also plotted: Caloi et al. (1997)[dotted line] and Salaris & Cassisi (1997, SC97) [solid line].

and

$$M_{Bol}^{Tip} = -(0.16 \pm 0.12)[M/H] - (3.78 \pm 0.14)$$

adopting the two metallicity scales, respectively.

For further comparisons with the models, two theoretical relations have been over-plotted in Fig.18: Caloi et al. (1997) (dotted line) and Salaris & Cassisi (1997, SC97) (solid line), respectively. They nicely agree each other and both define the upper boundary of the observations. It is important to remind here that the theoretical relationships have to be considered indeed as upper limits to the luminosity of the observed giants, because of the statistical fluctuations affecting these poor samples (Castellani, Degl'Innocenti, Luridana, 1993). On the other hand, it is also worth noticing that the bolometric magnitudes obtained from theoretical models are themselves affected by a quite large and systematic uncertainty ( $\geq 0.1$  mag), depending, among others, on the adopted bolometric correction for the Sun (Straniero 1999, private communication).

# 7.1. Uncertainties in the RGB tip determination

The procedure followed in order to compute the errors in the determination of the RGB tip magnitude deserves a brief description.

As demonstrated by Rood & Crocker (1997) a first order estimation of the statistical error  $(\sigma_{stat})$  in determining the RGB tip from a given sample of RGB stars, mainly depends on the sample size, being  $\sigma_{stat}^2 = 1/(\alpha(N+1)(N+2))$ , where N is the number of stars in the upper two bolometric magnitudes and  $\alpha$  is a parameter which depends on the rate of the RGB evolution. Its typical value is 0.04. In our sample of clusters  $\sigma_{stat}$  turns to be  $\leq 0.15$  mag. Only two clusters (namely M107 and M55), for which less than 10 stars in the upper two bolometric magnitudes of the RGB have been found, have larger scatters (0.39 and 0.26 mag, respectively). Of course, in order to compute the global uncertainty of the absolute magnitude,  $\sigma_{stat}$  has to be combined with the error in the determination of the distance modulus ( $\sim 0.2$  mag). The final errors on the bolometric RGB–Tip magnitude are listed in column 5 of Table 6. These errors have been conservatively assumed also for the  $M_K^{Tip}$  (see column 4 of Table 6).

# 8. Conclusions

A new set of high quality IR Color Magnitude Diagrams has been presented for a sample of 10 GGCs, spanning a wide range in metallicity. This new, homogeneous data-base has been used to determine a variety of observables quantitatively describing the main properties of the Red Giant Branch, namely: (a) the location of the RGB in the CMD (both in  $(J-K)_0$  and  $(V-K)_0$  colors at different absolute K magnitudes (-3, -4, -5, -5.5) and in temperature); (b) its overall morphology and slope; (c) the luminosity of the Bump and the Tip. All these quantities have been measured via a homogeneous procedure applied to each individual CMD. Their behavior as a function of the cluster metallicity has been investigated, also taking into account the effect of the  $\alpha$ -enhancement.

Comparisons with the most updated theoretical models show a substantial good agreement between observations and theoretical expectations, taking into account the errors and uncertainties still affecting both data and models.

In particular, it is interesting to note that the distance scale adopted in this paper (from F99), based on the theoretical luminosity of the ZAHB level, yields a very good agreement between the

observed features and the theoretical expectations along the RGB. If confirmed, this would indicate a high level of self–consistency of the theoretical RGB and ZAHB models, computed with the most up–dated input physics.

The relationships we present here can be used in further studies *i*) to derive a *photometric* estimate of the metal abundance from the RGB morphology and location, *ii*) to get useful distance estimates using both the RGB–tip and RGB–bump luminosities, and *iii*) to describe the overall behavior of the RGB properties in the near IR.

By coupling this IR study with our previous one on 61 GGCs in the V,B–V plane (cf. F99), a quite global scenario emerges, where the observational and theoretical descriptions start to match quite nicely if suitable multi–band photometric samples and up–dated models are used.

We warmly thank Oscar Straniero for making available the  $M_K$  magnitude of the RGB bump and tip from SCL97 models, and Bob Rood for the many instructive and useful discussions on theoretical models. The financial support of the "Ministero della Università e della Ricerca Scientifica e Tecnologica" (MURST) to the project Stellar Evolution is kindly acknowledged. FRF acknowledges the ESO Visitor Program for the hospitality.

## REFERENCES

Buonanno, R., Buscema, G., Corsi C.E., Ferraro, I., Iannicola, G., 1983, A&A, 126, 278

Buonanno, R., Iannicola, G., 1988, PASP, 101, 294

Caloi V., D'Antona F., Mazzitelli I., 1997, A&A 320, 823

Carney B.W., 1996, PASP 108, 900

Carretta E., Gratton R., 1997, A&AS 121, 95 (CG97)

Carretta, E., Gratton, R. G., Clementini, G., & Fusi Pecci, F. 1999, in press, (astro-ph 9902086)

Castellani, V., Degl'Innoconeti, S., Luridiana, V., 1993, A&A, 272, 442

Chaboyer, B., Demarque, P., Sarajedini, A., 1996, ApJ, 459, 558

Cohen J.C., Frogel, J.A., Persson, S.E., 1978, ApJ 222, 165

Cohen J.C., Sleeper C., 1995, AJ 109, 242 (CS95)

Crocker, D., A., Rood, R.T., 1984, in The Observational Tests of the Stellar Evolution Theory, eds A. Maeder and A. Renzini, Reidel, Dordrecht, p.159

Da Costa G.S, Armandroff T.E., 1990, AJ 100, 162

Davidge T.J., Simons D.A., 1991, AJ 101, 172

Davidge T.J., Simons D.A., 1994a, AJ 107, 240

Davidge T.J., Simons D.A., 1994b, ApJ 423, 640

Ferraro, F.R. 1992, MSAIt, 63, 491.

Ferraro, F.R., Clementini, G., Fusi Pecci, F., Buonanno, R., 1991, MNRAS, 252, 357

Ferraro F.R., Fusi Pecci F., Guarnieri M.D., Moneti A., Origlia L., Testa V., 1994a, MNRAS 266, 829

Ferraro F.R., Fusi Pecci F., Guarnieri M.D., Moneti A., Origlia L., Testa V., Ortolani S., 1994b, in McLean I.S., ed., Infrared Astronomy with Arrays: The next Genaration. Kluwer, Dordrecht, p.235

Ferraro F.R., Fusi Pecci, F., Testa, V., Greggio, L., Corsi, C.E., Buonanno, R., Terndrup, D.M., Zinnecker, H., 1995, MNRAS, 272, 391

Ferraro F.R., Messineo, M., Fusi Pecci, F., De Palo, M.A., Straniero, O., Chieffi, A., Limongi, M., 1999, AJ, 118, 1738 (F99)

Frogel J.A., Persson S.E., Cohen J.G., 1981, ApJ 246, 842

Frogel J.A., Cohen J.G., Persson S.E., 1983, ApJ 275, 773 (FCP83)

Fusi Pecci, F., Ferraro, F.R., Crocker, D., Rood, R.T., Buonanno, R., 1990, A&A, 238, 95.

Gratton R., Fusi Pecci F., Carretta E., Clementini G., Corsi C., Lattanzi M., 1997, ApJ 491, 749

Guarnieri, M.D., Ortolani, S., Montegriffo, P., Renzini, A., Barbuy, B., Bica, E., Moneti, A., 1998, A&A, 331, 70

Guarnieri, M.D., Renzini, A., Ortolani, S., 1997, ApJ, 477, 21

Harris, W.E., 1977, PASP, 89, 482.

Harris, W.E., 1996, AJ, 112, 1487.

Hartwick F.D.A., 1975, PASP 87, 77

Hartwick F.D.A., Sandage, A., 1968, ApJ, 153, 715

Iben, I. Jr., 1968, Nature, 220, 143

Kuchinski L.E., Frogel J.A., Terndrup D.M., Persson S.E., 1995, AJ 109, 1131 (K95)

Kuchinski L.E., Frogel J.A., 1995, AJ, 110, 2844 (KF95)

Minniti, D., 1995, A&A, 303, 468

Minniti, D., Olszewski, E.W., Rieke, M., 1995, AJ, 110, 1686

Montegriffo P., Ferraro F.R., Fusi Pecci F., Origlia L., 1995, MNRAS, 276, 739

Montegriffo P., Ferraro F.R., Origlia L., Fusi Pecci F., 1998, MNRAS, 297, 872

Moorwood A.F.M et al., 1992, The Messenger 69, 61

Origlia L., Ferraro F.R., Fusi Pecci F., Oliva E., 1997, A&A 321, 859

Ortolani S., Barbuy B., Bica E., 1991, A&A 249, L31

Pont, F., Mayor, M., Turon, C., VandenBerg, D.A., 1998, A&A, 329, 87

Reid, N., 1998, AJ, 115, 204

Renzini A., 1977, in Advanced Stages in Stellar Evolution, eds P. Bouvier and A. Maeder (Geneva), p. 149

Rood, R. T., Crocker, D. A. 1997, unpublished, http://www.astro.virginia.edu/~rtr/papers/

Rutledge, G.A., Hesser, J.E., Stetson, P.B., 1997, PASP, 109, 907

Salaris M., Cassisi S., 1997, MNRAS 289, 406 (SC97)

Salaris M., Cassisi S., 1996, A&A, 305, 858

Salaris M., Chieffi A., Straniero O., 1993, Mem. S.A.It. 63, 315

Straniero O., Chieffi, A., 1991, ApJS, 76, 911

Straniero O., Chieffi, A., Limongi, M., 1997, ApJ, 490, 425 (SCL97)

Sandage A., Katem B., 1964, ApJ 139, 1088

Van Den Berg, S., Younger, F., 1979, AJ, 84, 1305

VandenBerg, D.A., Stetson, P.B., Bolte, M., 1996, ARA&A, 34, 461

Zinn, R.J. 1980, ApJS, 42, 19.

Zinn, R.J. 1985, ApJ, 293, 424 (Z85)

Zinn, R.J., West, M.J. 1984, ApJS, 55, 45.

This preprint was prepared with an adapted version of the AAS IATEX macros v4.0.